Physics of Fluids

Fluvial instabilities

Cite as: Phys. Fluids **32**, 061301 (2020); https://doi.org/10.1063/5.0010038
Submitted: 07 April 2020 • Accepted: 12 May 2020 • Published Online: 02 June 2020

Subhasish Dey and Sk Zeeshan Ali

COLLECTIONS

This paper was selected as Featured

View Online Export Citation CrossMark

ARTICLES YOU MAY BE INTERESTED IN

Steady-state modeling of extrusion cast film process, neck-in phenomenon, and related experimental research: A review
Physics of Fluids **32**, 061302 (2020); https://doi.org/10.1063/5.0004589

On respiratory droplets and face masks
Physics of Fluids **32**, 063303 (2020); https://doi.org/10.1063/5.0015044

Likelihood of survival of coronavirus in a respiratory droplet deposited on a solid surface
Physics of Fluids **32**, 061704 (2020); https://doi.org/10.1063/5.0012009

Physics of Plasmas Physics of Fluids
Special Topic: Turbulence in Plasmas and Fluids
Submit Today!

AIP Publishing

© 2020 Author(s).

Physics of Fluids REVIEW scitation.org/journal/phf

Fluvial instabilities

Cite as: Phys. Fluids 32, 061301 (2020); doi: 10.1063/5.0010038
Submitted: 7 April 2020 • Accepted: 12 May 2020 •
Published Online: 2 June 2020

View Online Export Citation CrossMark

Subhasish Dey[1,2,a] and Sk Zeeshan Ali[3,b]

AFFILIATIONS

[1] Department of Civil Engineering, Indian Institute of Technology Kharagpur, West Bengal 721302, India
[2] Department of Hydraulic Engineering, State Key Laboratory of Hydro-Science and Engineering, Tsinghua University, Beijing 100084, China
[3] Department of Civil Engineering, Indian Institute of Technology Hyderabad, Telangana 502285, India

[a] **Author to whom correspondence should be addressed:** sdey@iitkgp.ac.in
[b] zeeshan@ce.iith.ac.in

ABSTRACT

Fluvial instabilities originate from an interplay between the carrier fluid and the erodible loose boundary at their interface, manifesting a variety of sedimentary architectures with length scales spanning from a few millimeters to hundreds of meters. This review sheds light on the current state-of-the-science of the subject, explaining the fluvial instabilities from three broad perspectives. They are micro-scale, meso-scale, and macro-scale instabilities. The interactions between the near-bed hydrodynamics and the sediment dynamics in generating various kinds of instabilities, including their natures and driving mechanisms, are thoroughly appraised in the light of laboratory experimental results, field observations, and theoretical backgrounds. Besides, this review addresses the current challenges, delineating key points as a future research scope.

Published under license by AIP Publishing. https://doi.org/10.1063/5.0010038

I. INTRODUCTION

Fluvial instabilities emerge from a direct interplay between a flowing fluid and an erodible boundary at their interface. They largely govern the dynamics of terrestrial terrains. The fluid shears the sediment grains to erode, giving rise to eclectic landforms, for instance, those in rivers, channels, and coastal areas. Fluvial instabilities span over a rich spectrum of spatiotemporal scales of sedimentary architectures. They can be broadly classified into three distinct categories: micro-scale, meso-scale, and macro-scale instabilities (Fig. 1),[1–6] depending on some typical physical system dimension (say, the wavelength λ of sedimentary architecture) that might range from a few millimeters to hundreds of meters. For instance, in micro-scale instabilities [Fig. 1(a)], wavelengths of sedimentary architectures are of the order of the flow depth h. Most common examples of such sedimentary architectures include chevron-shaped architecture [subpanel (i) of Fig. 1(a)], subaqueous ripples [subpanel (ii) of Fig. 1(a)] and dunes [subpanel (iii) of Fig. 1(a)], oscillating ripples [subpanel (iv) of Fig. 1(a)], and antidunes [subpanel (v) of Fig. 1(a)]. Note that subaqueous ripples are small asymmetrically triangular sedimentary architectures, formed in finer grains, having a long mild stoss-side slope (that is, flow facing slope) and a short steep leeside slope (that is, slip-slope). On the other hand, subaqueous dunes are large asymmetrical triangular architectures, formed in coarser grains, having a slight convexly curved mild stoss-side slope and a leeside slope, roughly equaling the angle of repose of sediments. However, recent research has evidenced that dunes in the world's large rivers are characterized by low-angle leeside slopes (<10°) and complex leeside shapes having the steepest portion close to the base of the leeside slope.[7] In addition, subaqueous antidunes are nearly sinusoidal sedimentary architecture, propagating upstream/downstream in a rapid flow.[2] In meso-scale instabilities, the wavelength is of the order of channel width B, for instance, large depositional patterns, called bars [Fig. 1(b)]. In addition, in macro-scale instabilities, the wavelength is proportional to some larger characteristic scale, say the valley width W. A well-known example is the evolution of a meandering channel through the landscape [Fig. 1(c)].

In a fluvial environment, two major kinds of sedimentary architectures prevail. The first kind corresponds to the evolutions of the streambed with streamwise and spanwise directions, where the former case leads to the formation of bedforms (e.g., ripples, dunes, and antidunes) and the latter to bars. On the other hand, the second kind of sedimentary architecture is related to the channel course

Published under license by AIP Publishing

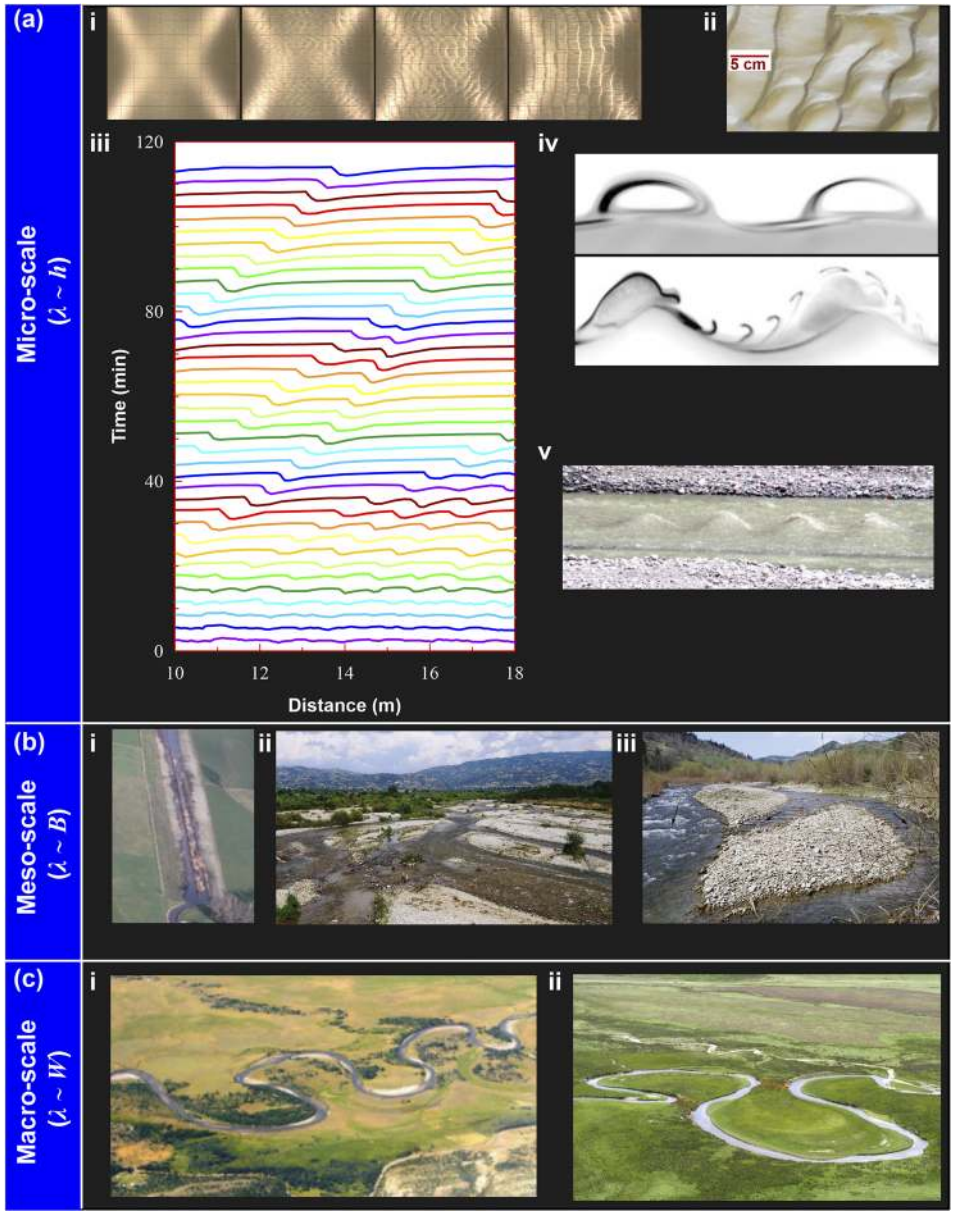

FIG. 1. Fluvial instabilities at different scales. (a) Micro-scale: (i) time evolutions of a plane bed (t = −60 s, −10 s, 30 s, and 240 s), leading to cross-hatch striations and chevrons.[1] Flow direction is from left to right. Before t = 0 s, the fluid flux was increased up to the desired flow. Grid spacing is 0.115 m. Reproduced with permission from Venditti *et al.*, "On interfacial instability as a cause of transverse subcritical bed forms," Water Resour. Res. **42**(7), W07423 (2006). Copyright 2006 John Wiley and Sons. (ii) Subaqueous ripples.[2] From Dey, *Fluvial Hydrodynamics: Hydrodynamic and Sediment Transport Phenomena*. Copyright 2014 Springer Nature. Reproduced with permission from Springer Nature. (iii) Spatiotemporal evolutions of subaqueous dunes.[3] (iv) Roll and roll-cum-jet patterns over a rippled bed created by oscillating flow.[4] Reproduced with permission from Ourmières and Chaplin, "Visualizations of the disturbed-laminar wave-induced flow above a rippled bed," Exp. Fluids **36**(6), 908–918 (2004). Copyright 2004 Springer Nature. (v) Subaqueous antidunes having a wavelength of 3 m on the Arveyron River.[5] Reproduced with permission from Recking *et al.*, "Antidunes on steep slopes," J. Geophys. Res.: Earth Surf. **114**(F4), F04025 (2009). Copyright 2009 John Wiley and Sons. (b) Meso-scale: (i) alternate bars in a tributary of the River Meuse.[6] Reproduced with permission from Eekhout *et al.*, "Field experiment on alternate bar development in a straight sand-bed stream," Water Resour. Res. **49**(12), 8357–8369 (2013). Copyright 2013 John Wiley and Sons. (ii) Gravel bars in a braided river.[2] From Dey, *Fluvial Hydrodynamics: Hydrodynamic and Sediment Transport Phenomena*. Copyright 2014 Springer Nature. Reproduced with permission from Springer Nature. (iii) Dissected bar in a river.[2] From Dey, *Fluvial Hydrodynamics: Hydrodynamic and Sediment Transport Phenomena*. Copyright 2014 Springer Nature. Reproduced with permission from Springer Nature. (c) Macro-scale: (i) aerial photograph of the Simpson River near Balmaceda.[2] From Dey, *Fluvial Hydrodynamics: Hydrodynamic and Sediment Transport Phenomena*. Copyright 2014 Springer Nature. Reproduced with permission from Springer Nature. (ii) Potentiality of cutoff (shown by red broken lines) in a meandering river.[2] From Dey, *Fluvial Hydrodynamics: Hydrodynamic and Sediment Transport Phenomena*. Copyright 2014 Springer Nature. Reproduced with permission from Springer Nature.

Published under license by AIP Publishing

over the landscape (e.g., a meandering channel). These sedimentary architectures are manifested owing to the instabilities of the basic unperturbed flow in a straight channel. The driving mechanism of fluvial instabilities is essentially governed by the fluid energetics, eroding the sediments from the channel boundary.

In the past few decades, remarkable advances were made in understanding the basic processes of fluvial instabilities. These processes were largely studied through analytical, experimental, and numerical frameworks. From the perspective of the formation of fluvial sedimentary architecture, particular attention has been given on the development of bedforms,[8] their stability in the light of experimental and field observations,[9] dynamical mechanisms of ripples and dunes,[10,11] morphology of alluvial rivers,[12] free and forced fluvial sedimentary structures,[13] and formation of channel patterns.[14] This review aims to provide an understanding of the current state-of-the-science of fluvial instabilities, offering an insight into the near-bed hydrodynamics that plays an important role in the instability mechanism over large spatiotemporal scales. It emphasizes how small perturbations owing to a change in flow variables affect the stability of a fluvial system. This article is organized as follows: In Sec. II, the micro-scale instabilities are discussed, highlighting certain concepts of their formation, controlling factors, driving mechanisms, and modeling strategies. Section III is devoted to meso-scale instabilities, where linear and nonlinear stability analyses of fluvial bars are reviewed. The macro-scale instabilities are presented in Sec. IV, discussing the subtle role of nonlinear effects, for instance, channel width variations [subpanel (i) of Fig. 1(c)] and cutoff dynamics [subpanel (ii) of Fig. 1(c)]. Finally, Sec. V presents a brief summary of the review, highlighting key points to be addressed as a future research scope.

II. MICRO-SCALE INSTABILITIES

A. Onset of streambed erosion: Instability at grain scale

Let us first visualize a situation,[15–17] where a turbulent flow passes over a plane streambed comprising loosely and/or closely packed bed sediment grains, as conceptually sketched in Fig. 2. The flow exerts a shear stress τ_0 on the surface of bed grains. Initially, let us assume τ_0 to be much smaller than its threshold limit τ_{0c} so that the grains maintain a stable equilibrium. Now, a crucial question arises: how do the grains respond to a small perturbation (an increase in τ_0) imposed on the streambed? The same question can be put forward in a slightly different way—what are the decisive factors in governing the streambed stability? Over the decades, researchers attempted to find a satisfactory answer to this stirring question, unveiling couple of key factors that might precisely describe the onset of streambed erosion.[18] Some of them include grain properties (grain size, shape, and roughness), streambed features (grain protrusion, packing conditions, grain sorting, and streambed slope), and flow and turbulent characteristics (flow depth, flow velocity, velocity, and pressure fluctuations). Note that the condition $\tau_0 \geq \tau_{0c}$ suggests an unstable equilibrium, featuring three distinct modes of grain entrainment, such as rolling, sliding, and lifting modes (Fig. 2). In particular, the hydrodynamic drag F_D and lift F_L are the destabilizing forces, while the submerged weight F_G of the grain provides the stabilizing force. In a rolling mode, the destabilizing moment M_D, created by F_D and F_L, about the pivoting point surpasses the stabilizing moment M_S about that point. It follows: $M_D \geq M_S$. In a sliding mode, the hydrodynamic drag F_D exceeds the tangential frictional resistance F_R at the contacts, yielding $F_D \geq F_R$. In addition, in a lifting mode, the hydrodynamic lift F_L exceeds the submerged weight F_G of the grain, producing $F_L \geq F_G$. Recent studies have evidenced that the flow velocity at the onset of streambed instability is closely linked with the energetics of turbulent eddies, preserving universal scaling laws, called *Ali–Dey's law of the entrainment threshold*, over a wide range of grain sizes.[19,20] Among the celebrated schools of thoughts on the subject, the onset of streambed erosion has been envisioned as a state that provides the maximum stability to the grains, beyond which the grains are entrained into the flow. It turns out that the onset of streambed erosion is not an abrupt phenomenon rather a transition from a stable bed to an erodible bed.

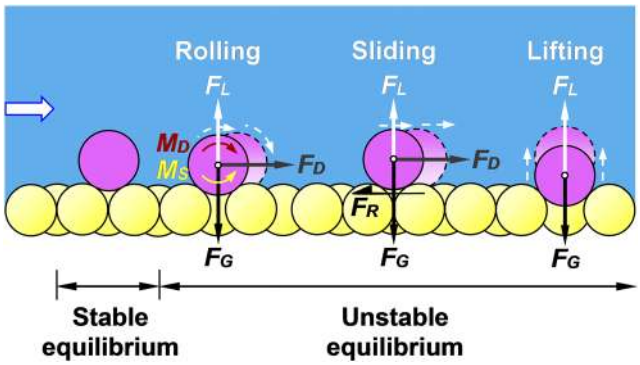

FIG. 2. Conceptual sketch of instability at grain scale, highlighting stable and unstable equilibria. Broken arrows represent various modes of grain entrainment. Flow direction shown by an arrow is from left to right.

B. Sedimentary architecture

Beyond the threshold limit ($\tau_0 > \tau_{0c}$), the plane streambed becomes unstable owing to the motion of grains at the bed surface, displaying various kinds of sedimentary architecture [Fig. 1(a)]. Their dimensions (shape, size, and spacing) are largely guided by the flow depth, flow velocity, and size and grading of grains. Fluvial bedforms are categorized in accordance with their chronological appearance into three distinct flow regions that are governed by the flow Froude number F $[=U/(gD)^{1/2}]$, where U is the depth-averaged flow velocity, g is the gravitational acceleration, and D is the hydraulic mean depth (ratio of the flow cross-sectional area to the top width).[2] In a tranquil flow ($F < 1$), sedimentary architectures consist of ripples, ripples on dunes, and dunes. In a transitional flow ($F \approx 1$), washout dunes appear. On the other hand, in a rapid flow ($F > 1$), sedimentary architectures include plane bed, antidunes, and chutes and pools.[2] Note that chutes and pools are sedimentary architectures, being found at relatively steep streambed slopes. Chute, formed by large extended sediment heaps, carries a shooting flow that rushes into a pool, where a tranquil flow prevails. The fluvial bedforms (excluding antidunes that can also propagate upstream) generally propagate in the downstream with a propagation speed quite smaller than the average flow velocity.

Published under license by AIP Publishing

C. Genesis of fluvial bedforms

The genesis of fluvial bedforms is based on the multifarious features of near-bed instabilities. Particularly, two distinct modes of bedform inception have been evidenced in laboratory measurements—defect and instantaneous inception.[1,21] The former is associated with bed defects propagating streamwise and spanwise directions with the aid of flow separation. It occurs at smaller flow strengths, where bed sediment motion is random and patchy. The latter takes place instantaneously at larger flow strengths over the entire bed when sediment motion follows a general transport. This kind of bedform inception on a plane streambed starts with the impression of a cross-hatch pattern, leading to chevrons [subpanel (i) of Fig. 1(a)]. Next, we discuss the role of near-bed hydrodynamics and some phenomenological concepts of bedform instability (interfacial Kelvin–Helmholtz type instability and two-stage concepts) to gain an insight into the genesis of fluvial bedforms.

1. Near-bed hydrodynamics

With regard to fluvial bedforms, the near-bed hydrodynamics was extensively explored through experimental observations and numerical simulations.[22–30] It has been well-documented that near-bed turbulent sweeps play a delicate role to initiate the instability of a plane sand bed. As the turbulent sweeps interact with the streambed, they trigger high fluid momentum toward the bed, producing a fluctuating shear stress field that remains spatially heterogeneous.[23,24] Regions of high concentration of shear stress fluctuations spontaneously result in local erosion of grains on a micro-scale over the entire bed, and the eroded grains are eventually deposited nearby. Therefore, the cross-hatch striations and chevrons emerging on the bed are directly linked with the near-bed turbulent sweeps prior to a further destabilization of the bed.

2. Interfacial Kelvin–Helmholtz type instability concept

Liu[31] reported that a streambed could be thought of as a viscous fluid so that the ripples could evolve as a result of the interfacial Kelvin–Helmholtz type instability of two sheared fluids having different mass densities [Fig. 3(a)]. The interface between two fluids with mass densities ρ_1 and ρ_2, and velocities u_1 and u_2, respectively, is unstable if

$$(u_1 - u_2)^2 > \frac{1}{2\pi\rho_1\rho_2} gL(\rho_2^2 - \rho_1^2), \tag{1}$$

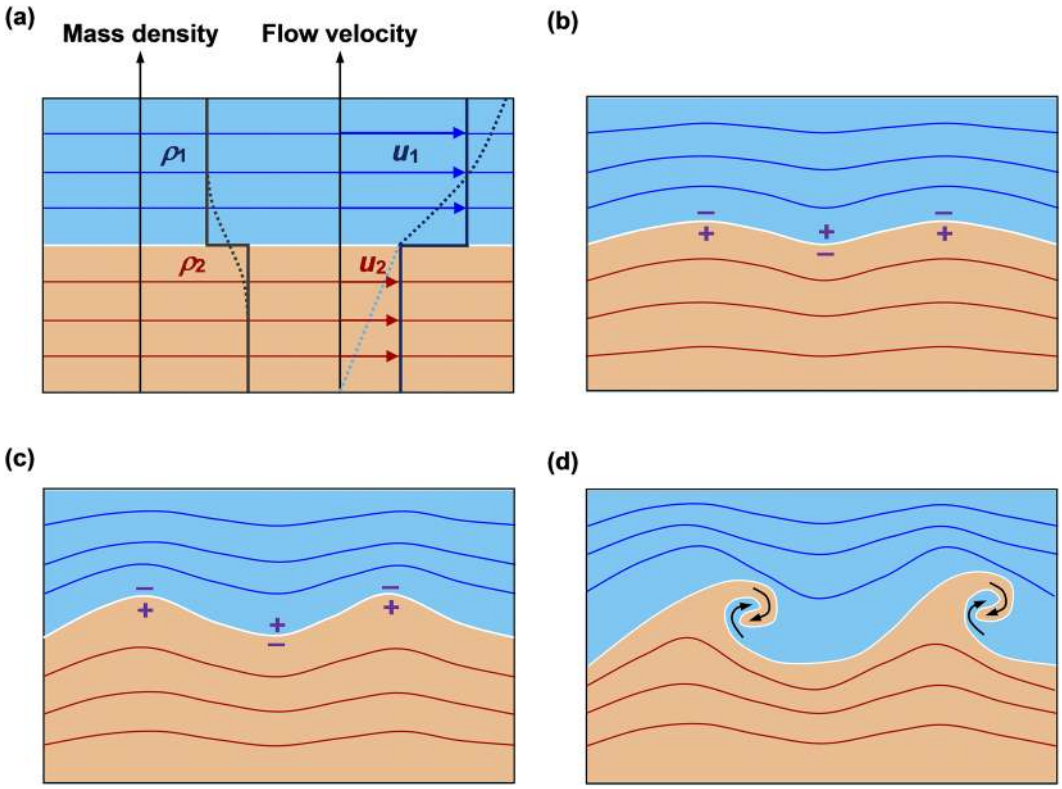

FIG. 3. Conceptual sketch of time evolution of bedforms, explained by the Kelvin–Helmholtz type instability at the density interface (white line) between two fluids. (a) Idealized profiles of mass density and streamwise flow velocity are shown by solid lines, while the actual profiles are indicated by dotted lines. (b) Variation in streamwise flow velocity yields convergence and divergence of flow streamlines, resulting in wavy patterns on the interface. An increase in velocity is balanced by a reduction in pressure intensity, and vice versa (Bernoulli principle). The plus (minus) symbol shows increased (reduced) pressure intensity across the interface. (c) Further growth of bedforms as variations in pressure intensity are enhanced with time. (d) Vorticity concentration at the bedform crests and the evolution of distinct spanwise vortices.

Published under license by AIP Publishing

where L is the Kelvin–Helmholtz wavelength. In essence, a wide variety of interfacial instabilities may emerge depending on the Richardson number J in the range $-3 \le J \le 1$. The J is expressed as $J = \Delta\rho g\delta/(\rho_2 \Delta u^2)$, where $\Delta\rho$ and Δu are the mass density and velocity differences, respectively, and δ is the velocity interface thickness. In particular, the Kelvin–Helmholtz instability for flow over a sand bed dominates for $J < 0.07$. It turns out that the onset of bed instability can be linked with the Kelvin–Helmholtz type waves that arise owing to the stratification effects at the sediment–water interface, resulting from large suspended sediment concentration. Variation in streamwise flow velocity across the interface produces acceleration and deceleration of flow streamlines, resulting in a pressure contrast to form undular patterns on the interface [Fig. 3(b)]. The undular patterns further accentuate with time [Fig. 3(c)]. Finally, the hydrodynamic instability imprints large localized striations of erosion and deposition, creating propagating bedforms [Fig. 3(d)]. Experimental observations have evidenced that an instantaneous inception of bedforms is driven by an interfacial instability.[1] This reveals that the near-bed turbulent mechanism may not be required in explaining the inception of bedforms—a contradictory finding to the origin of fluvial bedforms grounded on the role of turbulent coherent structures. Numerical simulation of an oscillating flow over a sand bed strongly evidenced that the stratification effects have a pivotal role to initiate the formation of bedforms.[32] Specifically, it was found that when the stratification effects are overlooked in the momentum balance, ripples do not arise as an outcome of numerical simulation. By contrast, in the absence of stratification effects, the formation of ripples from a plane bed has been well-documented.[33] Recent large-eddy simulation models have demonstrated that the stratification effects are important at later stages (after the formation of cross-hatch and chevron patterns), particularly when the near-bed turbulent sweeps are to entrain the grains effectively into suspension forming a heterogeneous stratified layer just above the streambed.[24]

3. Two-stage concept

Experimental observations have revealed that regular seed waves (initial regular waves, being originated from the granular motion over a plane bed, from which quasi-equilibrium dunes are eventually evolved) are created in a two-stage process,[34] as sketched in Fig. 4. In the first stage, random interactions of sediment patches of varying length scales (typically 7–15 times the grain size d) take place over the plane mobile bed, providing corridors of sediment transport events induced by the attached turbulent eddies. As the speed of attached eddies scales with their length scales,[35] larger eddies produce stronger sediment transport events. As a consequence, eddy transport events in conjunction with the moving grains propagate at speeds that scale with their size, in contrast to the inverse scaling law observed for the propagation of already developed larger seed waves.[36] When the interactions of the moving sediment patches over the plane bed generate disturbances exceeding a threshold height H (~3–4 times the grain size d), the bedload layer is disturbed and the disturbance amasses sediments (Fig. 4). In the second stage, regular patterns of seed waves are formed downstream of the stabilized disturbance in succession through a scour-deposition wave, resulting from the demand of sediment continuity, and the bed shear stress and sediment flux distributions downstream of the perturbed bed. The maximum bed shear stress $\tau_0|_{max}$ is located at a distance of 30–40 times the threshold height H downstream of the stabilized bed disturbance (Fig. 4).

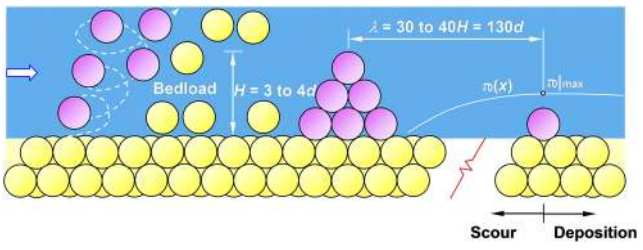

FIG. 4. Conceptual sketch of the two-stage concept.

D. Controlling factors

The factors driving the evolutions of micro-scale instabilities include fluid and granular variables (Fig. 5). Several limiting curves offer a clear distinction of various kinds of bedforms. In Fig. 5(a), the mean flow velocity U at 10 °C temperature of water as a function of median grain size d in the range of fine sands to medium gravels is shown.[37] However, to capture more salient features of such evolutions, fluid and granular variables can be coupled together to form a set of nondimensional groups. Four key nondimensional parameters are shown in Figs. 5(b)–5(d). They are Shields parameter Θ $[=\tau_0/(\rho_g - \rho_f)gd]$, shear Reynolds number R_* $(=u_* k_r/\upsilon)$, grain parameter D_* $\{=d[(\rho_g/\rho_f - 1)g/\upsilon^2]^{1/3}\}$, and movability parameter M_* $(=u_*/w_s)$, where ρ_g and ρ_f are the mass densities of grains and fluid, respectively, u_* is the shear velocity $[= (\tau_0/\rho_f)^{1/2}]$, k_r is the grain roughness height (proportional to grain size d), υ is the coefficient of the kinematic viscosity of fluid, and w_s is the grain settling velocity. The evolutions of bedforms on $\Theta(R_*)$, $D_*(R_*)$, and $M_*(R_*)$ planes provide a good understanding of the required conditions for their formation [Figs. 5(b)–5(d)]. However, the $\Theta(R_*)$ diagram of Chabert and Chauvin[38] is unable to capture the sedimentary architecture in a rapid flow, such as antidunes [Fig. 5(b)]. By contrast, the $D_*(R_*)$ diagram of Bechteler *et al.*[39] elucidates that for finer grains ($D_* < 20$), there is a transition from ripples to plane bed in a rapid flow followed by antidunes that are formed with an increase in R_* [Fig. 5(c)]. For coarser grains, dunes follow a thin strip of plane bed in a tranquil flow. The transition from ripples to dunes (ripples superimposed on dunes) is confined to a shaded triangular region. In addition, the $M_*(R_*)$ diagram of Simons and Richardson[40] encompasses a broad range of grain sizes (very fine sand to small cobble) [Fig. 5(d)]. In this context, it is worth emphasizing that Naqshband *et al.*[41] experimentally studied the transition from dunes to plane bed in a rapid flow under nonequilibrium conditions. The transition of dunes was found to be governed by the position of the peak sediment transport rate with respect to the dune crest. The sediment transport distributions indicated a positive phase lag distance between the dune crest and the peak sediment transport rate, ultimately leading to washout dunes. The phase lag distance was found to be approximately three-fourths of the flow depth, corroborating theoretical predictions. The bedload, captured in dune troughs, was found to contribute to the translation of dunes and most of the suspended

Published under license by AIP Publishing

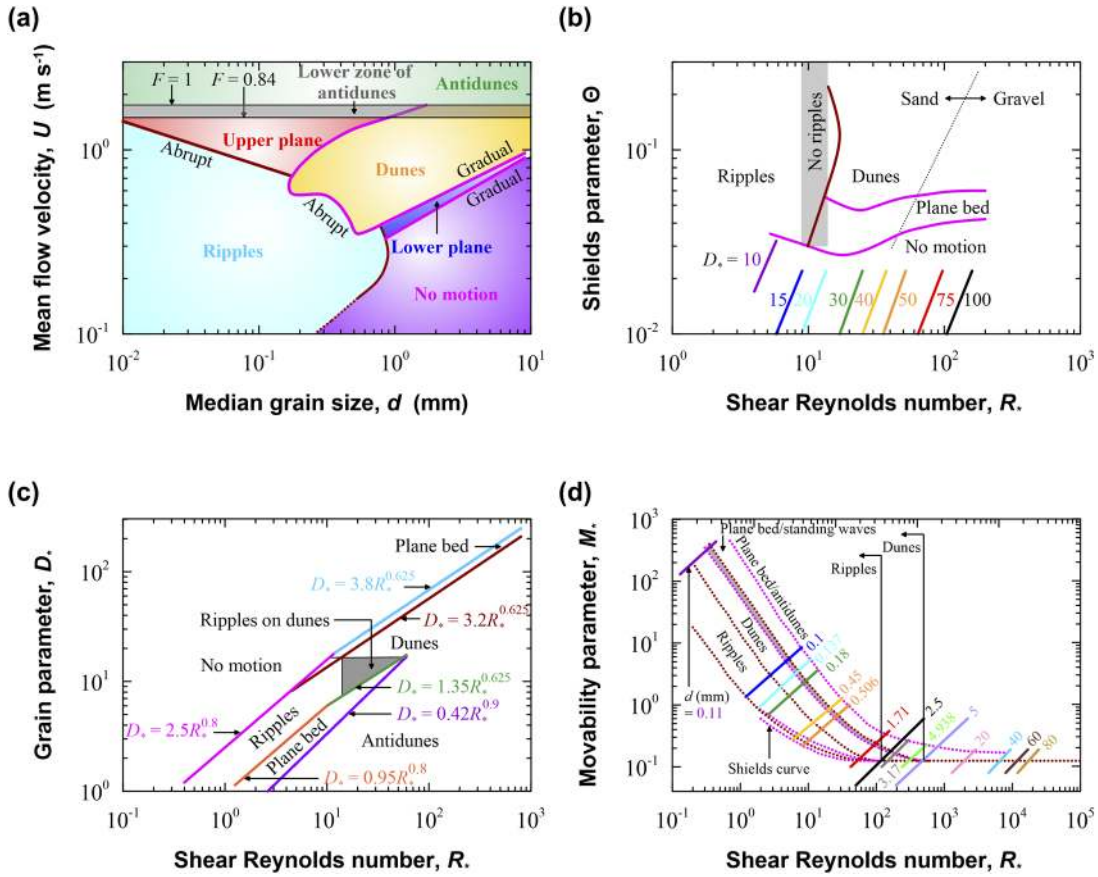

FIG. 5. Evolutions of fluvial bedforms governed by characteristic parameters: (a) mean flow velocity U vs median grain size d,[37] (b) Shields parameter Θ vs shear Reynolds number R_*,[38] (c) grain parameter D_* vs shear Reynolds number R_*,[39] and (d) movability parameter M_* vs shear Reynolds number R_*.[40]

load to propagate downstream, contributing to the deformation of dunes.

The effects of grain sorting play an important role in the formation of some fluvial bedforms.[42] The grain sorting is a process, where the selective transport of various fractions of a sediment mixture results in a nonuniform probability distribution of the grain size. In particular, the effects of grain sorting significantly control the formation of bedload sheets and sand ridges. However, fluvial dunes and bars were found to be moderately affected by the sorting mechanism.

The bedform predictor diagrams (Fig. 5) rely mostly on cohesionless sediments, although most subaqueous environments comprise mixtures of cohesionless sand, cohesive mud, and extracellular polymeric substances (EPS) produced by microorganisms. Therefore, an understanding of the role of cohesive and biologically active sediments in influencing the sediment transport is a key prerequisite to explore the bedform dynamics in aquatic environments.[43,44] The experimental study of Malarkey *et al.*[43] revealed that the time required for the development of bedforms enhances by two orders of magnitude for a very small amount of pervasively distributed EPS. This effect was found to be stronger than for physical cohesion because the EPS hinder the independent movement of sand grains. The presence of EPS was found to reduce bedform dimensions and steepness.[44] Baas *et al.*[45] reported that the subaqueous ripples in sand grow at a slower rate if cohesive sediments (clay) are added to the sand. As the clay content increases, the ripples gradually become smaller, switching from the three-dimensional (3D) to two-dimensional (2D) structure. However, compared to clay, the EPS strongly affect the size of ripples.

E. Driving mechanism

In this section, we describe how the micro-scale instabilities (in the context of fluvial bedforms) propagate over space-time. First, fluid and granular conservation laws are succinctly discussed, highlighting the pivotal role of frictional effects. Then, simple kinematic considerations are illustrated to explain the driving mechanism.

1. Conservation laws

The schematic illustration of flow over dunes is given in Fig. 6(a), where x and z are the coordinates whose origin lies at a convenient point. The sediment flux continuity equation linking the

Published under license by AIP Publishing

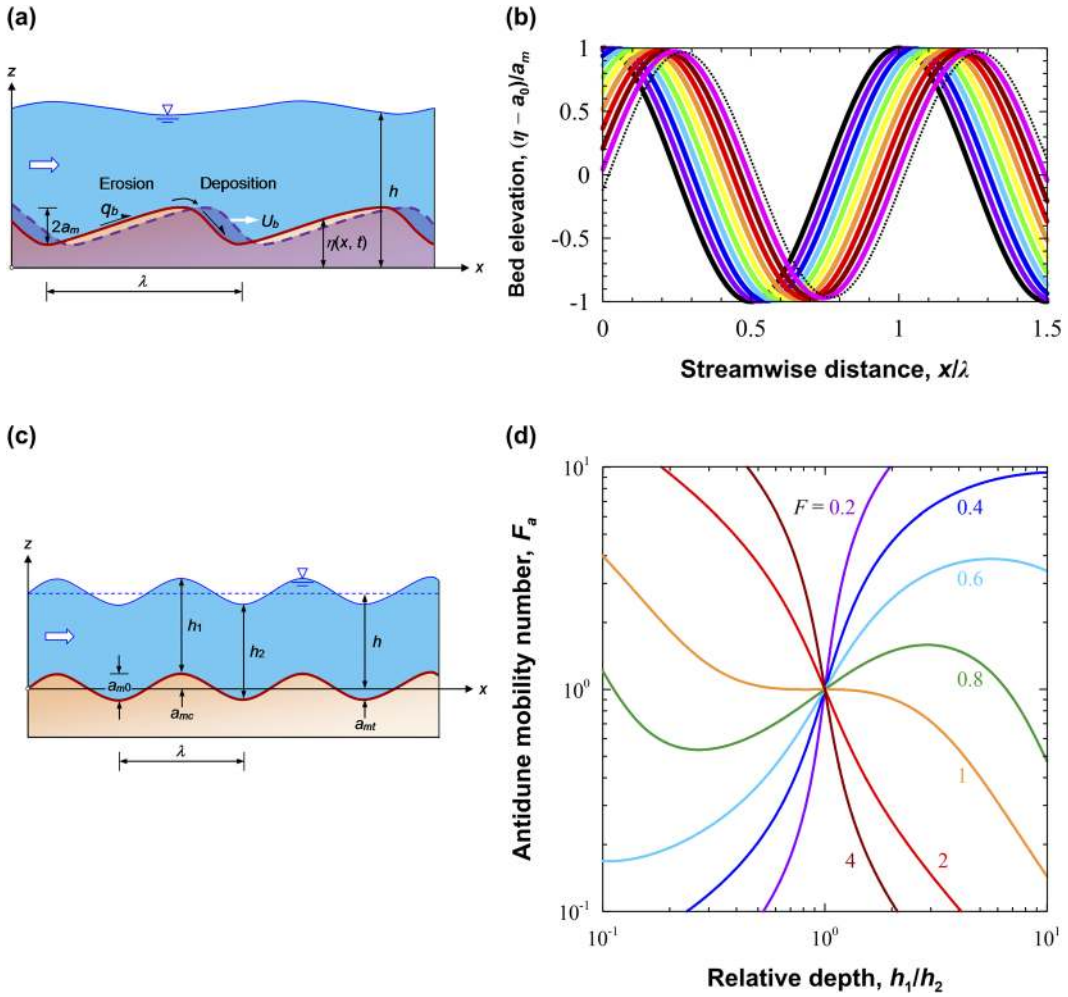

FIG. 6. (a) Schematic illustration of dune instability, aided by erosion and deposition of grains over stoss-side and leeside, respectively. Dunes propagate downstream with a speed U_b. (b) Time evolutions of bed elevation, $(\eta - a_0)/a_m$ propagating downstream for the first 10 s (with an interval of 1 s), computed from the Exner equation.[46] The black solid line denotes the profile at $t = 0$, while the dotted line corresponds to the profile at $t = 10$ s. (c) Schematic illustration of flow over antidunes to highlight the antidune mobility. (d) Antidune mobility number F_a vs relative depth h_1/h_2.

spatiotemporal bed profile $\eta(x, t)$ and the grain flux $q_g(x, t)$ per unit channel width at an arbitrary time t follows the Exner equation,[46]

$$\frac{\partial q_g}{\partial x} = -(1 - \rho_0)\frac{\partial \eta}{\partial t} - \frac{\partial}{\partial t}\int_{\eta}^{h} c\,dz, \tag{2}$$

where ρ_0 is the porosity of grains and $c(x, z, t)$ is the concentration of suspended grains. The dominant modes of sediment transport in morphodynamic modeling are the bedload and suspended load. Their underlying mechanics and modeling strategies were reviewed elsewhere.[47,48] However, when the effects of sediment suspension are negligible, the total grain flux in Eq. (2) can be solely considered to be the bedload flux. Exner[46] expressed the bedload flux q_b as $q_b = (1 - \rho_0)U\alpha_E$, where α_E is the erosion coefficient. From the flow continuity, the fluid flux q per unit width is $q = U(h - \eta)$, where h is the free surface elevation from the horizontal reference level [Fig. 6(a)]. At $t = 0$, the bed profile can be assumed to be $\eta = a_0 + a_m \cos(k_w x)$, where a_m is the half-amplitude and k_w is the wavenumber of bedforms (inversely proportional to the wavelength λ). The solution of Eq. (2) can be expressed as $\eta = a_0 + a_m \cos[k_w(x - U_b t)]$,[46] where U_b is the propagation speed of bedforms $[=\alpha_E q/(h - \eta)^2]$. This expression demonstrates that the bedform crest travels faster than the trough, resulting in an asymmetrical wave with a mild stoss-side slope [see subpanel (iii) of Fig. 1(a)]. Nevertheless, this analytical solution was reported to anticipate an unrealistic overhanging bedform crest portion (on the leeside) with time.

When frictional effects are considered, the dynamic equation of flow reads[2]

$$S_f = S_0 - \frac{\partial h}{\partial x} - \frac{1}{g}\left(U\frac{\partial U}{\partial x} + \frac{\partial U}{\partial t}\right), \tag{3}$$

Published under license by AIP Publishing

where S_f is the friction slope and S_0 is the streambed slope. Considering a horizontal bed ($S_0 = 0$) and approximating the frictional effects as $gS_f \approx k_f U$ (k_f is the friction parameter per unit time),[46] Eq. (2) produces

$$\frac{\partial^2 \eta}{\partial t^2} - m_0 \frac{\partial^2 \eta}{\partial x \partial t} + k_f \frac{\partial \eta}{\partial t} - \alpha_E g \frac{\partial^2 \eta}{\partial x^2} = 0, \tag{4}$$

where $m_0 = gqU^{-2} - U$. The solution of this equation, subject to the initial condition $\eta(x, 0) = a_0 + a_m \cos(k_w x)$, produces[46]

$$\eta = a_0 + a_m \exp\left[-\left(\frac{k_f}{2} - p\right)t\right] \cos\left\{k_w\left[x - \frac{m}{2p}\left(\frac{k_f}{2} - p\right)t\right]\right\}, \tag{5}$$

where $p = k_f/2 - \beta$ and β is a characteristic parameter. The β can be obtained by solving the following quartic equation:

$$4\beta^4 - 8k_f\beta^3 + [5k_f^2 + (m^2 + 4\alpha_E g)k_w^2]\beta^2 - [k_f^3 + (m^2 + 4\alpha_E g)k_f k_w^2]\beta + \alpha_E g k_f^2 k_w^2 = 0. \tag{6}$$

Figure 6(b) shows the evolutions of bedforms obtained from the Exner model[46] for characteristic values $\lambda = 3$ m ($k_w = 2.09$ m^{-1}), $m = 18.12$, $\alpha_E = 1.67 \times 10^{-4}$, and $k_f = 1.67 \times 10^{-3}$. The reason for selecting the above characteristic values is that they offer preliminary guidelines to represent the bedforms in either laboratory or prototype scale. Importantly, the condition $\beta > 0$ reveals that the amplitude of bedforms gradually decreases as time increases owing to the frictional effects. The propagation speed and the rate of decrease in amplitude of shorter wavenumber bedforms are also slower than the longer ones.

2. Kinematic considerations

Simplified continuity and energy equations of flow over bedforms can be applied to find their propagation direction and speed. Song[49] expressed the propagation speed of bedforms as $U_b = U^2(\partial q_b/\partial U)[q(1 - F^2)]^{-1}$. This expression reveals that since $\partial q_b/\partial U > 0$ (bedload flux increases as the flow velocity increases), the propagation direction is solely controlled by the flow Froude number. Therefore, bedforms propagate downstream (upstream) if $F < 1$ ($F > 1$)—a condition that corroborates experimental observations. In essence, for flow over antidunes [subpanel (v) of Fig. 1(a)], the antidunes propagate downstream if the grains are eroded over the stoss-side and eventually deposited over the leeside. By contrast, they propagate upstream for the otherwise scenario.[50] For flow over an idealized train of sinusoidal antidunes [Fig. 6(c)], the energy balance, considering frictional effects to be negligible, between the upstream section (at the crest) and the downstream section (at the trough) produces

$$a_{mc} + h_1\left(1 - \frac{U_1^2}{gr_1}\right) + \frac{U_1^2}{2g} = -a_{mt} + h_2\left(1 + \frac{U_2^2}{gr_2}\right) + \frac{U_2^2}{2g}, \tag{7}$$

where a_{mc} and a_{mt} are the elevations of crest and trough from a fixed reference level and r is the radius of curvature.[50] For symmetrical antidunes, Fig. 6(c) suggests that $a_{m0} = 2a_{mc} = 2a_{mt}$ and $r = r_1 = r_2 = 2/(a_{m0}k_w^2)$. For stationary (non-propagating) antidunes, the above energy balance yields the antidune mobility number F_a to be unity ($F_a = 1$). Note that the antidune mobility number is defined as the product of flow Froude number, mean flow depth, and wavenumber ($=Fhk_w$). With these considerations, the energy balance results in a quadratic equation of F_a as

$$A_1 F_a^2 + A_2 F_a + A_3 = 0, \tag{8}$$

where

$$A_1 = \frac{\pi}{\lambda} a_{m0} F \left(\frac{h_2}{h_1}\right)^{1/2}\left(1 + \frac{h_1}{h_2}\right),$$
$$A_2 = \frac{1}{2}F^2\left(\frac{h_1}{h_2} - \frac{h_2}{h_1}\right) - \left[\left(\frac{h_1}{h_2}\right)^{1/2} - \left(\frac{h_2}{h_1}\right)^{1/2}\right], \tag{9}$$
$$A_3 = -\frac{2\pi}{\lambda} a_{m0} F.$$

Figure 6(d) illustrates the variations of antidune mobility number F_a with relative depth h_1/h_2 for different flow Froude numbers F. It appears that for $F > 1$ (rapid flow where antidunes occur), F_a is <1 (>1) if $h_1/h_2 > 1$ (<1). Thus, the criterion for the propagation direction of antidunes can be set as follows: antidunes propagate downstream (upstream) if $F_a < 1$ (>1).

F. Linear stability analysis

The linear stability analysis has been established to serve as a key tool in anticipating fluvial instabilities. After the pioneering work of Kennedy[51] on the subject, the evolutions of both 2D and 3D bedforms were studied from three different perspectives—the potential flow model, the de Saint-Venant type model (shallow water model), and the rotational flow model.

It is worth noting that the potential flow model does not offer any bed shear stress.[8,51] Therefore, a phase lag distance l_s is often introduced, either artificially or by considering the subtle role of sediment suspension, in generating the instability. Figure 7 shows how the stable, unstable, and neutral regions are created depending on the values of the nondimensional phase lag $k_w l_s$ and flow

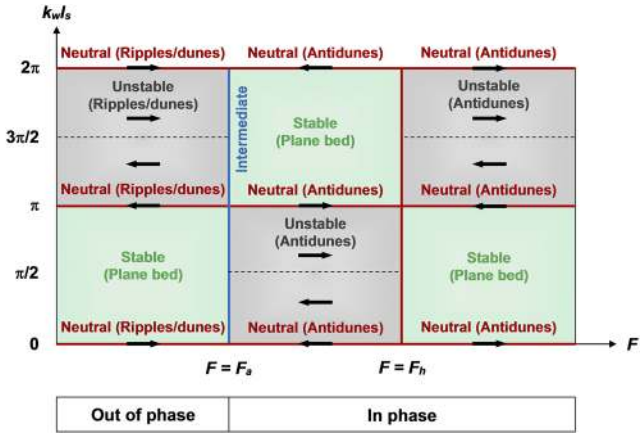

FIG. 7. Schematic illustration of stable (green), unstable (gray), and neutral (red) regions on the $k_w l_s(F)$ plane. F_a and F_h denote two limiting values of the flow Froude number. Stable regions manifest a plane bed, while neutral and unstable regions give rise to both ripples/dunes and antidunes. Rightward (leftward) arrows represent the propagation direction in downstream (upstream). Note that at $F = F_a$ (blue line), stability is intermediate. The bed and free surface profiles are out of phase (in phase) if $F < F_a$ ($F > F_a$),

Published under license by AIP Publishing

Froude number F. In fact, these regions manifest various kinds of bed configurations (plane bed, ripples/dunes, and antidunes) and their propagation directions. In Fig. 7, two limiting values of the flow Froude number are expressed as $F_a^2 = \tanh(k_w h)/(k_w h)$ and $F_h^2 = 1/[k_w h \tanh(k_w h)]$. For ripples/dunes, the bed and free surface profiles are out of phase, whereas for antidunes and plane bed, these profiles are in phase (Fig. 7). In essence, for slowly varying amplitude of bedforms, the wavenumber k_w corresponding to the maximum initial growth rate can be related to the flow Froude number F as follows:[51]

$$F^2 = \frac{1 + k_w h \tanh(k_w h) + k_w l_s \cot(k_w l_s)}{(k_w h)^2 + [2 + k_w l_s \cot(k_w l_s)] k_w h \tanh(k_w h)}. \quad (10)$$

Figure 8(a) provides the solution of Eq. (10) for different values of the relative phase lag distance l_s/h, showing various kinds of bed configurations on the $F(k_w h)$ plane. In addition, several limiting curves, obtained from the potential theory,[51] are highlighted. Among the limiting curves, F_m, F_b, F_1, and F_2 are expressed as

$$F_m^2 = \frac{1}{k_w h}, \; F_b^2 = \frac{\cosh^2(k_w h)}{k_w h[k_w h + \sinh(2k_w h)]}, \quad (11)$$

$$\begin{pmatrix} F_1^2 \\ F_2^2 \end{pmatrix} = \frac{1}{4k_w h \tanh(k_w h)} \{C + 2 \pm [(C+2)^2 - 8C\tanh^2(k_w h)]^{1/2}\}, \quad (12)$$

where $C = (a/l_s) \times (2g/U^2)$ and a is a phenomenological coefficient.[52] In the inset of Fig. 8(b), the propagation of antidunes in upstream (downstream) is shown by solid (dotted) lines. For $F \in [F_a, F_h]$, antidunes propagate upstream (downstream) if $0 < k_w l_s < \pi/2$ ($\pi/2 < k_w l_s < \pi$), suggesting that their propagation direction changes at $k_w l_s = \pi/2$ (see also Fig. 7).

The drawback of the potential flow model can be resolved by using the de Saint-Venant type model, which considers frictional effects.[53] However, the de Saint-Venant type model is applicable to predict the meso-scale instabilities, where the streamwise wavelength is much larger than the flow depth. It turns out that although such a model is capable of shedding light on the alternate bar formation,[54] it does not offer much insights into the mechanisms of subaqueous dunes and antidunes for which a rotational flow model seems to be promising.[13]

On the other hand, the rotational flow model can provide a precise estimation of the bed shear stress,[10,55–61] stemming from an eddy viscosity and a slip-velocity concept. Using the vorticity transport equation and considering the role of sediment suspension, a 2D linear stability analysis of an erodible bed was proposed.[62,63] In contrast to using a constant eddy-viscosity approach, Richards[56] reported two distinct modes of instability in a hydraulically rough flow regime. In the first mode, the instability induced wavelength patterns scale with the bed roughness, giving rise to the formation of ripples, while in the other mode, the wavelength scales with the flow depth, producing dunes. Two central factors were identified, such as the bed roughness length and the effects of the local streambed slope on bedload transport. Sumer and Bakioglu[57] incorporated the effects of viscosity on the formation of bedforms by considering the vanishing flow Froude number limit. It was found that the wavelength of ripples scales with the viscous sublayer thickness rather than the bed roughness. Based on the Reynolds-averaged Navier–Stokes equations, Bose and Dey[53] analyzed the stability of bedforms and provided the stable and unstable regions on the $F(k_w h)$ plane [gray lines in Fig. 8(a)]. They found $F = 0.177$ to be the lower limit of bedform formation [dashed horizontal line in Fig. 8(a)]. In another attempt, Bose and Dey[64] predicted the formation of ripples, considering their subtle influence on the near-bed thick fluid layer, which spans up to 3.5 times the ripple height. The computed ripple length scaled by its size was found to increase with an increase in Shields parameter. The rotational flow model also offers an understanding of the formation of 2D and 3D bedforms.[61]

Colombini and Stocchino[65] analyzed the linear stability of ripples and dunes, extending earlier theories to hydraulically smooth

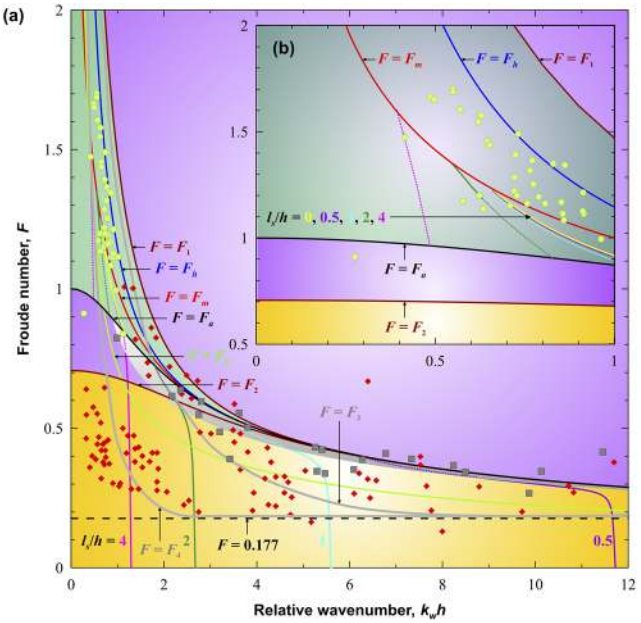

FIG. 8. (a) Flow Froude number F vs relative wavenumber $k_w h$ for dunes (diamonds), antidunes (circles), and plane bed (squares).[2] Regions of occurrence of various bed configurations for different values of the relative phase lag distance l_s/h (= 0, 0.5, 1, 2, and 4), obtained from the potential theory,[51] are shown. Distinct shaded areas of occurrence of dunes (yellow), plane bed (purple), and antidunes (green), obtained from the modified potential theory,[52] are highlighted. The solid gray and dashed horizontal lines represent two limiting curves of instability, obtained from the turbulent flow model.[53] *Kennedy's predictions:* $F = F_a$ is the smallest flow Froude number for the occurrence of antidunes (or the largest flow Froude number for the occurrence of dunes) and $F = F_m$ is the largest flow Froude number for the occurrence of long-crested patterns. For $F < F_a$, solid lines for different values of l_s/h correspond to ripples and dunes, while dotted lines refer to transition. The transition region is shown in gray. $F = F_b$ is the limiting curve when the phase lag originates from phase shifts between the bed movements and flow properties. *Hayashi's predictions:* Dunes (antidunes) occur for $F < F_2$ ($F > F_1$), while the plane bed occurs for $F_2 < F < F_1$ and $F > F_1$. The unstable region is confined to $F = F_a$ and $F = F_h$. *Bose and Dey's predictions:* The region confined to $F = F_3$ and $F = F_4$ is unstable, while regions beyond these curves are stable. (b) Propagation of antidunes (above $F = F_a$), given by Kennedy.[51] The solid (dotted) lines for different values of l_s/h correspond to the upstream (downstream) propagation of antidunes.

Published under license by AIP Publishing

and transitional flow regimes. In hydraulically smooth and transitional flow regimes, both ripples and dunes emerge as a primary instability. This observation is contradictory to the findings of Fourrière *et al.*,[66] who found that ripples are formed owing to the primary instability, while dunes are driven by the nonlinear pattern coarsening. Recently, Duran Vinent *et al.*[67] reported a numerical model of the formation of subaqueous ripples and dunes in the limit of infinite flow depth. The underlying mechanism of instability, for both the formation of ripples and dunes, is the phase lag between the bed shear stress and the volumetric sediment flux. The key factors that affect the phase lag are summarized in Sec. II G.

G. Factors influencing phase lag

The phase lag varies substantially in the vicinity of the bed. Colombini[58] argued that since the bedload layer has a finite thickness, the fluid stress perturbations resulting in the bedload transport could be determined at the top of the bedload layer. The phase lag depends on several key factors, for instance, the effects of fluid friction, suspended sediments, gravity, and grain inertia. These aspects are briefly furnished below.

The first key factor is the effect of fluid friction that greatly influences the phase lag at a smaller shear stress, where the bedload remains the predominant mode of sediment transport. Upstream (downstream) of the bedform crest, the flow is accelerated (decelerated), producing a larger (smaller) bed shear stress compared to the uniform flow.

When the bed shear stress increases further, the amount of suspended sediments is enhanced, contributing positively to the phase lag. The maximum suspended sediment transport takes place downstream of the position of the maximum bed shear stress. This indicates that in a tranquil flow, the suspended sediments have a positive contribution to the phase lag. It follows that for a larger bed shear stress where the suspended load dominates the bedload, the positive contribution from the suspended sediments exceeds the negative contribution from the frictional effects. This fact explains the transition from dunes to a stable plane bed configuration.

The effects of the local streambed slope on bedload transport remain another aspect to govern the instability at a smaller bed shear stress. Fredsøe[63] reported that the gravity plays a delicate role in the formation of dunes. In essence, when the effects of the local streambed slope are considered, the dune obliquity is increased considerably.[63] However, Fredsøe's[63] analysis was grounded on the slip-velocity concept, which drastically underestimates the bed shear stress. However, when a more promising flow model was used,[56] it was revealed that the strength of the stabilizing effects owing to the gravity is much larger than Fredsøe's[63] idealistic assumption.

In a tranquil flow, the phase lag owing to the grain inertia is positive.[68] On the other hand, in a rapid flow, it is negative, resulting in an unstable bed. When bedload transport remains the primary mode of sediment transport, the grain inertia results in the formation of antidunes for small flow depths to carry coarser grains. In essence, for sand bed streams, the contribution from sediment suspension to the phase lag exceeds that from grain inertia, and as a consequence, the effects of grain inertia on the phase lag become trivial. However, Colombini[58] found that the antidunes could be formed in the absence of suspended sediments without considering the effects of grain inertia.

Andreotti *et al.*[69] found that in a tranquil flow, the instability yields ripples (or chevrons) depending on the effects of the free surface. In fact, the ratio of the saturation length to the flow depth governs the transition from spanwise to oblique bedforms. Furthermore, in a rapid flow, this ratio controls the transition from ripples to antidunes. Antidunes are evolved in the neighborhood of resonance for free surface waves—a condition that leads to the destabilization of the sediment transport saturation. Andreotti *et al.*[69] also anticipated the appearance of anti-chevrons (oblique bedforms propagating upstream) at large flow Froude numbers.

H. Convective/absolute nature of instability

Fundamentally, a physical system is convectively unstable if the response of the system to an impulsive perturbation grows with time but migrates and falloffs to zero at all spatial positions. It suggests that a convectively unstable system acts as a noise amplifier, exhibiting the extrinsic dynamics of the system because the response declines to zero in the absence of continuous forcing. On the other hand, a physical system is absolutely unstable, if the response of the system increases exponentially with time at all spatial positions. Therefore, an absolutely unstable system behaves as an oscillator, displaying the intrinsic dynamics of the system. It reveals the fact that in a convectively unstable system, Green's function reduces asymptotically to zero along $x/t = 0$, while in an absolutely unstable system, Green's function tends to infinity.

Vesipa *et al.*[70] unveiled that the dune instability is convective in nature for all the physical control parameters, whereas the antidune instability displays both the convective and absolute behaviors depending on the choice of control parameters. They also reported that the relative roughness (ratio of the grain size to the flow depth) has a minor role in determining the convective/absolute nature of bedform instability. Bohorquez and Ancey[71] considered a proper choice of grain diffusivity in the flow model to

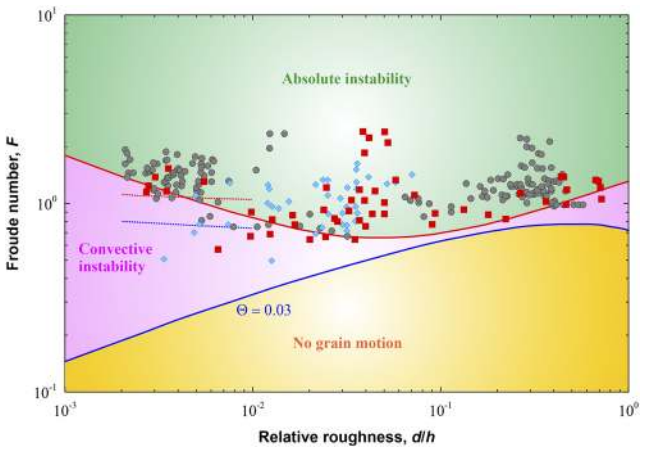

FIG. 9. Flow Froude number F vs relative roughness d/h, highlighting the regions of convective and absolute instabilities,[71] for 2D upstream propagating antidunes (gray circles), 3D downstream propagating antidunes (blue diamonds), and standing waves (red squares). The solid limiting lines are Bohorquez and Ancey's[71] predictions. The dotted lines (blue and red) are the neutral curves, obtained by Vesipa *et al.*,[70] for the onset of convective and absolute instabilities.

Published under license by AIP Publishing

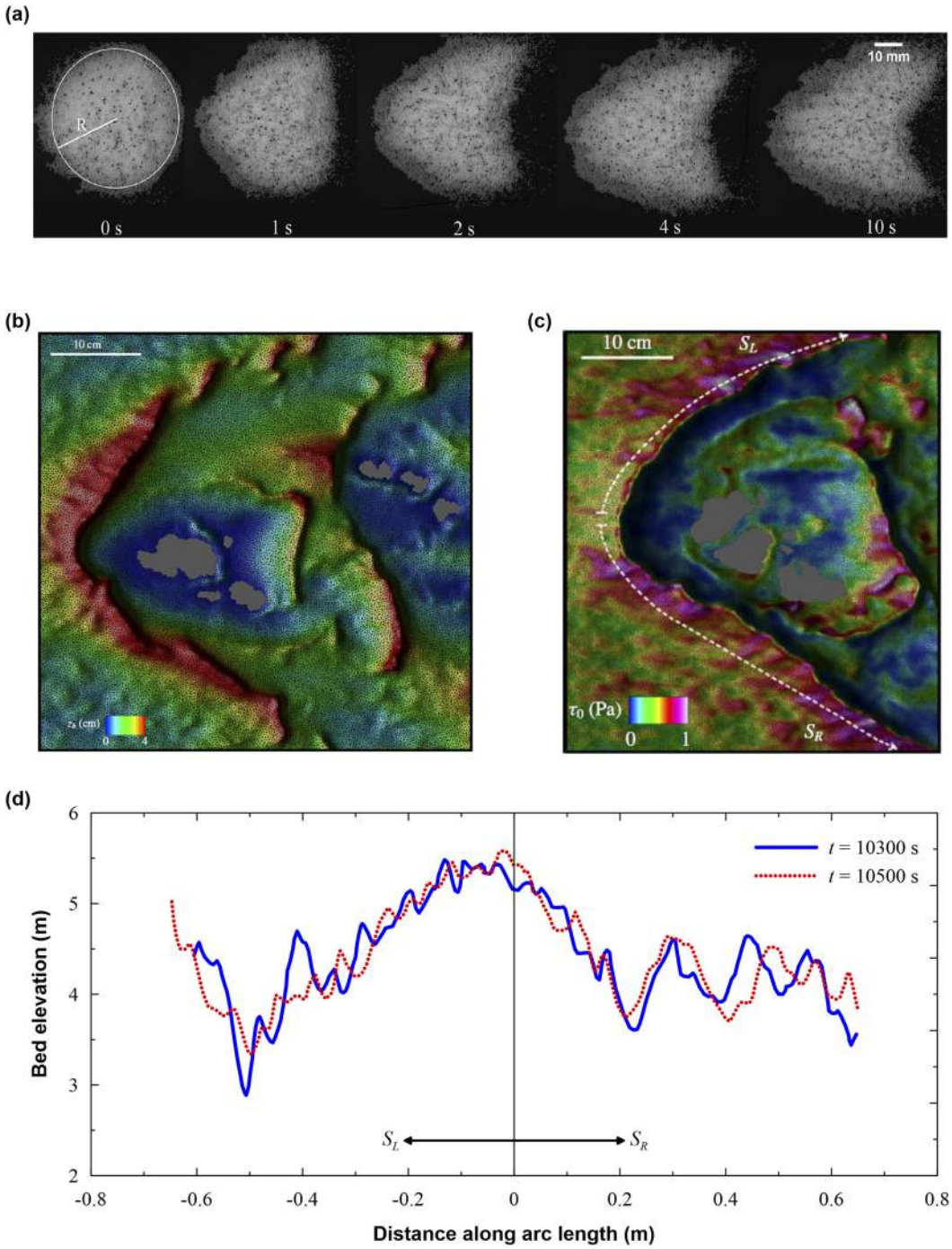

FIG. 10. (a) Formation of subaqueous barchans in a laboratory environment,[72] showing the deformation of a conical heap of radius R at various instances (flow direction is from left to right). Reproduced with permission from Alvarez and Franklin, "Role of transverse displacements in the formation of subaqueous barchan dunes," Phys. Rev. Lett. **121**(16), 164503 (2018). Copyright 2018 American Physical Society. (b) Simulated dynamics of the 3D bed elevation plot at t = 8200 s displaying the calving process (unstructured triangular grids for discretizing the bed are in black). The gray portions illustrate the exposed bedrock.[73] Reproduced with permission from Khosronejad and Sotiropoulos, "On the genesis and evolution of barchan dunes: Morphodynamics," J. Fluid Mech. **815**, 117–148 (2017). Copyright 2017 Cambridge University Press. (c) Contours of bed shear stress at t = 10 600 s (equilibrium state).[73] Reproduced with permission from Khosronejad and Sotiropoulos, "On the genesis and evolution of barchan dunes: Morphodynamics," J. Fluid Mech. **815**, 117–148 (2017). Copyright 2017 Cambridge University Press. (d) Bed profiles along the arc length S [shown by a white dashed line in (c)] for t = 10 300 s and 10 500 s.[73]

Published under license by AIP Publishing

anticipate the onset of absolute instability for antidunes over a broad range of relative roughness (Fig. 9). Vesipa *et al.*[70] obtained the transition from convective to absolute instability for $F \geq 1$ and $d/h \leq 3.5 \times 10^{-3}$. The curve defining the onset of absolute instability for antidunes, obtained by Bohorquez and Ancey,[71] has a good qualitative congruence with that of Vesipa *et al.*[70]

I. Criticisms on the linear stability analysis

The assumptions in the linear stability analysis are valid in the initial stages of the formation of sand dunes and ripples (mostly rolling grain ripples) because during this period, the amplitude of bedforms remains small. The rolling grain ripples correspond to the sand ripples above which the flow separation does not produce vortices and the bedload transport remains the predominant mode of sediment transport in destabilizing the plane bed.[32] However, the initial period prevails only for the first few minutes. Therefore, it is quite smaller than the characteristic time scale of a bedform life cycle, spanning from several hours to days. When the bedforms grow adequately in amplitude and wavelength, an enhanced shear stress owing to an accelerated flow over the stoss-side together with the flow separation from the leeside provides the mechanism for entrainment and deposition of grains, resulting in the geometrical growth of bedforms. Once this state is reached, the linear models no longer apply.[32] Such a feature is quite common for subaqueous barchans.[72] In this context, it is worth highlighting the formation and stability of subaqueous barchans. Barchans, a special type of sand dune [Fig. 10(a)], are featured by their distinguished crescentic shape, including a stoss-side, two horns pointing downstream, and a slip surface on the leeside. In particular, they are formed in unidirectional flow when the sand supply on the bedrock is limited. Specifically, the dynamics and the associated bed instabilities giving rise to subaqueous barchans were explored in the literature.[24,73] Khosronejad and Sotiropoulos[73] reported the detailed processes of collision and merging of faster moving small sand masses with slower moving large sand masses to form the first barchanoid. The collision and merging processes take place continuously over time and offer the principle mechanism for the evolution of the barchan field. However, as time progresses toward a quasi-equilibrium state, the above processes do not end up with a single mega-barchan dune, rather a process called calving becomes prominent [Fig. 10(b)], where spanwise sand waves destabilize the barchans horns, creating small-scale dunes. Therefore, calving provides the sand-loss mechanism to stop barchanoids from growing forever. When the grown-up barchans attain an equilibrium size, they become large enough in carrying a sizable amount of sand along their horns and central curved portion. It turns out that as the flow approaches the stoss-side, it is accelerated and diverted toward the horns. The augmented shear stress acting on the curved surface destabilizes the sand bed [Fig. 10(c)], producing spanwise ripples that cover the whole stoss-side surface. The ripples propagate from the center of the barchan toward its horns, creating an irregular rippled surface of the barchan dunes [Fig. 10(d)]. As soon as the barchans grow to a significant size, they destabilize the neighboring flow, creating surface waves. Interestingly, once the surface waves travel up to the tip of the horn, they destabilize it readily, producing shedding of new small-scale dunes of various sizes and propagation speeds from the horns of the parent dunes.

Another criticism concerning the linear stability analysis is that the theoretical predictions support the experimental data in the long-term, where the dynamics is controlled primarily by nonlinear effects. However, they fail surprisingly at the initial stages, where a linearized approach is more likely owing to small perturbations.[74] In the long-term, the rolling grain ripples tremendously grow in size, called the vortex ripples, allowing vortices to form over the leeside. The vortices produce a strong vertical velocity field entraining sediments into the flow. As a result, the suspended sediment transport becomes the key mode of sediment transport because the grains are ejected into the flow by a strong vertical velocity field associated with the near-bed turbulence. Under such circumstance, the linear stability analysis fails owing to the presence of suspended load, which governs the transition from rolling grains to vortex ripples.[32]

III. MESO-SCALE INSTABILITIES

Meso-scale instabilities produce various kinds of fluvial bars [Fig. 1(b)]. Bars can be classified into two broad categories—free and forced bars. Free bars emerge from the instability of a streambed, whereby any small perturbation of bed elevation increases with time [subpanel (i), Fig. 1(b)]. On the other hand, forced bars arise owing to forcing effects, for instance, variation in channel width, channel curvature, and nonuniform initial conditions. To be specific, in a meandering channel, the channel curvature triggers a secondary current, giving rise to periodic regions of erosion (deposition) at outer (inner) bends [subpanel (i) of Fig. 1(c)]. These features bear a resemblance to alternate bars with an exception of their non-propagating behavior. An in-depth review of fluvial bars, in the light of theoretical and numerical modeling, and experimental and field observations, has recently been reported elsewhere.[75]

It is worth discussing that the alternate bars in a straight channel can be propagating or non-propagating. Olesen[76] found that the alternate bars having the largest growth rate propagate rapidly, leading to a uniform erosion of channel banks rather than a local bank erosion. This observation results in a channel widening rather than a meandering. Previously, it was thought that the alternate bars are non-propagating if the channel width to flow depth ratio remains at the resonance, or if they are forced by a local perturbation. However, performing a 2D numerical modeling together with a laboratory experiment, Crosato *et al.*[77] reported that the bars in a straight channel can be non-propagating without the aforementioned conditions. They found that both the non-propagating bars in a straight channel with non-erodible banks and the onset of meandering of a straight channel with erodible banks are inherent responses of the channel bed without requiring a resonance condition or a forced steady upstream perturbation. The nature of the two inherent responses can, however, be different. The non-propagating bars between non-erodible channel banks originate from the mild growth of a marginally stable non-propagating mode of bed topography. On the other hand, the meanders and the related non-propagating bars between erodible channel banks are caused by local bank erosion at the initial pools of propagating alternate bars.

A. Convective nature of bar instability

Formation of alternate bars in a straight channel has been widely explained by the normal mode stability analysis.[78] The physical system is shown in Fig. 11(a). Let (U, V) be the streamwise and

Published under license by AIP Publishing

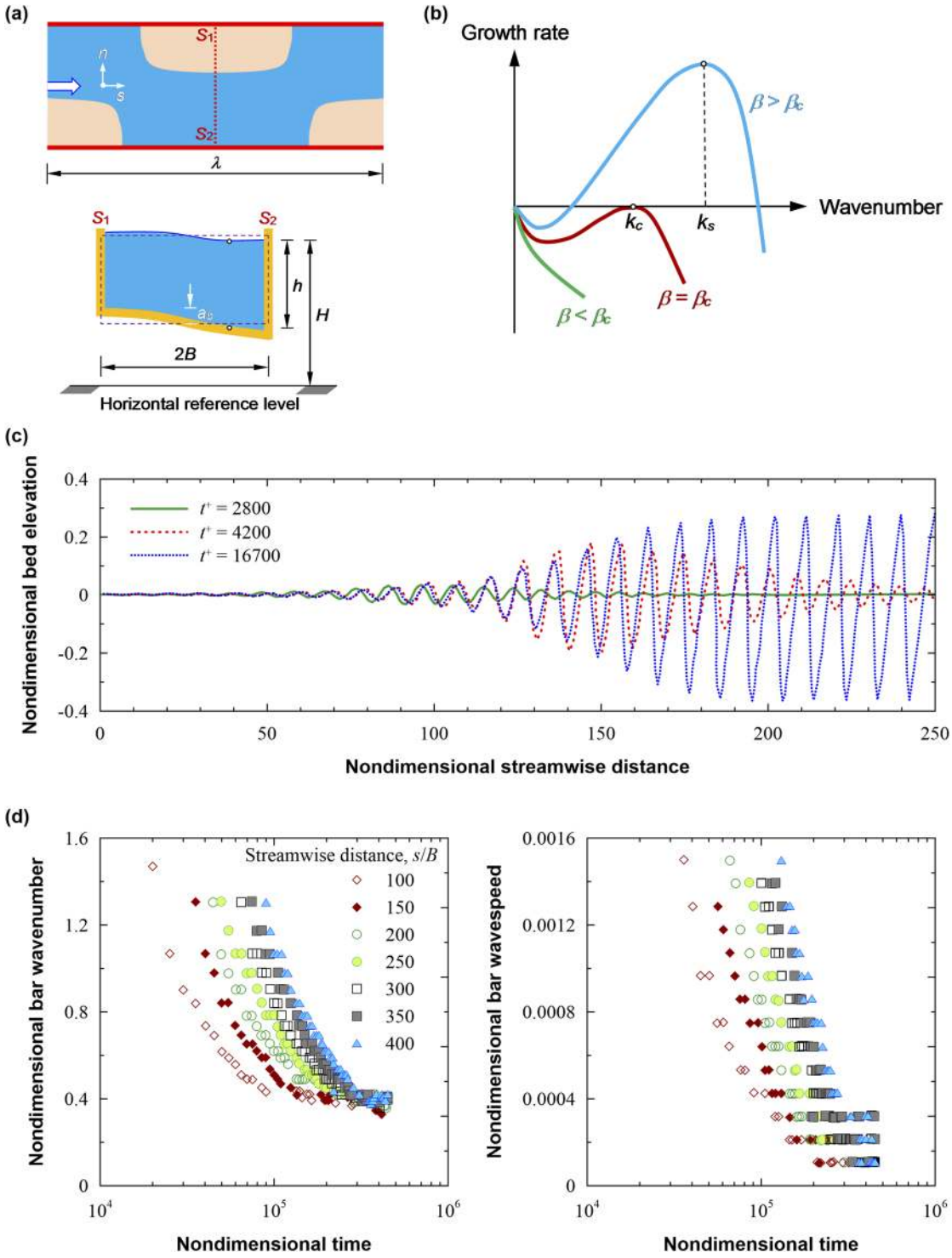

FIG. 11. (a) Schematic illustration of alternate bar formation in a straight channel. (b) Bar growth rate vs bar wavenumber, illustrating three typical scenarios of aspect ratio. (c) Simulated spatiotemporal evolutions of bed elevation, $(H - h)/h_0$ at the right bank for $\Theta = 0.057$, $d/h_0 = 0.053$, $\beta = 8$, and $\beta_c = 5.6$. Here, the streamwise distance and time are made nondimensional by channel half-width B and $B/(\varepsilon U_0)$, respectively, U_0 is the uniform flow velocity, and ε is the ratio of hydrodynamic to morphodynamic time scales (run "1Freq" in Ref. 80). Evolutions of bed elevation are shown for three values of nondimensional time, $t^+ = 2800$, 4200, and 16 700. (d) Spatiotemporal evolutions of bar wavenumber and propagation speed for $\Theta = 0.057$, $d/h_0 = 0.053$, $\beta = 8$, and $\beta_c = 5.6$ (run "20Freq" in Ref. 80).

Published under license by AIP Publishing

spanwise velocity components with respect to the Cartesian coordinate system (s, n). In the cross-sectional view, the channel width is $2B$, and h and H denote the local flow depth and elevation of the free surface from a fixed datum, respectively. We introduce $(\hat{s}, \hat{n}) = (s/B, n/B)$, $(\hat{U}, \hat{V}) = (U, V)/U_0$, U_0 being the unperturbed streamwise velocity, $\hat{H} = H/(h_0F^2)$, $F = U_0/(gh_0)^{1/2}$, $\hat{h} = h/h_0$, $\hat{t} = tU_0/B$, and variables with subscript "zero" refer to the unperturbed state. In the stability analysis, the following linearization technique is applied:

$$(\hat{U}, \hat{V}, \hat{H}, \hat{h}) = (1, 0, \hat{H}_0, 1) + \varepsilon[(\hat{U}_1, \hat{V}_1, \hat{H}_1, \hat{h}_1) + \text{c.c.}], \tag{13}$$

where ε is a small quantity, c.c. denotes the complex conjugate, and the set of variables $(\hat{U}_1, \hat{V}_1, \hat{H}_1, \hat{h}_1)$ is expressed as[78]

$$(\hat{U}_1, \hat{V}_1, \hat{H}_1, \hat{h}_1)\Big|_{m=\text{odd}} = \exp(\hat{\Omega}\hat{t})[S_m(\hat{n})\tilde{U}_1, C_m(\hat{n})\tilde{V}_1, S_m(\hat{n})\tilde{H}_1, S_m(\hat{n})\tilde{h}_1]E_1(\hat{s}, \hat{t}), \tag{14}$$

$$(\hat{U}_1, \hat{V}_1, \hat{H}_1, \hat{h}_1)\Big|_{m=\text{even}} = \exp(\hat{\Omega}\hat{t})[C_m(\hat{n})\tilde{U}_1, S_m(\hat{n})\tilde{V}_1, C_m(\hat{n})\tilde{H}_1, C_m(\hat{n})\tilde{h}_1]E_1(\hat{s}, \hat{t}), \tag{15}$$

$$S_m(\hat{n}) = \sin\left(\frac{1}{2}\pi m\hat{n}\right),\ C_m(\hat{n}) = \cos\left(\frac{1}{2}\pi m\hat{n}\right),$$

and

$$E_m(\hat{s}, \hat{t}) = \exp mi(k\hat{s} - \hat{\omega}\hat{t}). \tag{16}$$

In the above, $\hat{\Omega}$, k, and $\hat{\omega}$ denote the nondimensional growth rate of perturbation, wavenumber ($=2\pi B/\lambda$), and angular frequency, respectively, and m represents the bar mode. In particular, $m = 1$ corresponds to the formation of alternate bars. It may be noted that there remains a clear distinction between the alternate bars and the diagonal bars. The diagonal bars are often regarded as 3D dunes. In this regard, the rotational flow model of Colombini and Stocchino[61] is worth highlighting, where the stability analysis offered a precise distinction between them.

Figure 11(b) shows a conceptual representation of the bar growth rate as a function of nondimensional bar wavenumber k. It appears that when the aspect ratio β ($=B/h_0$, where h_0 is the uniform flow depth) attains its threshold value ($\beta = \beta_c$), perturbation of wavenumber $k = k_c$ yields a neutral condition (perturbation neither grows nor decays with time). On the other hand, for $\beta < \beta_c$ ($\beta > \beta_c$), perturbations decay (grow) with time, ensuring the stability (instability) of a plane bed. The latter essentially describes the condition for the alternate bar formation with a wavenumber k_s of maximum instability [Fig. 11(b)]. In the stability analysis, the basic state is perturbed by adding infinitesimal perturbations, which are substituted into the governing equations to find a system of perturbed equations that can be solved, subject to boundary conditions and suitable closure relationships. It is pertinent to point out that the effects of flow unsteadiness influence the instantaneous bar growth rate and govern the final amplitude of the bed configuration.[79]

Particularly, it was revealed that the nature of bar instability is convective,[80] making use of the properties of branch singularities. Numerical simulations of a fully nonlinear problem showed that groups of bars, emanating either from an arbitrarily distributed or a localized bed topography perturbation, grow and propagate downstream keeping the source area unaffected. The spatiotemporal evolution of bottom elevation along the right-side channel bank confirms a nonlinear saturation [Fig. 11(c)], indicating that the spatiotemporal amplification essentially attains an equilibrium amplitude. In addition, as the bars approach to the nonlinear regime, their wavelength enhances, while their propagation speed reduces [Fig. 11(d)].

B. Effects of sediment suspension

The effects of sediment suspension have been reported to alter the bar instability significantly. However, bar instability remains convective in the presence of sediment suspension.[81] In the linear stability analysis of Federici and Seminara,[81] effects of sediment suspension were considered by means of an asymptotic approach, proposed by Bolla Pittaluga and Seminara.[82] On the other hand, Bertagni and Camporeale[83] proposed a weakly nonlinear model by applying the center manifold projection technique. In fact, sediment suspension offers a destabilizing mechanism in governing bar instability. It affects both the bar wavenumber in the linear analysis [Fig. 12(a)] and the bar amplitude in weakly nonlinear analysis [Fig. 12(b)]. The presence of sediment suspension is to increase the instability region by diminishing the threshold aspect ratio β_c and the threshold wavenumber k_c [Fig. 12(a)]. It essentially leads to longer bars under the threshold condition. Bertagni and Camporeale[83] validated the outcomes of both the linear and nonlinear analyses with a few field observations of alternate bars available in the existing literature, for instance, the Mississippi River, the artificial channel in The Netherlands, and the Yellow River. In one of the field observations, the effects of sediment suspension were important in identifying the bar instability, whereas for the remaining field observations, the inclusion of sediment suspension was found to increase the accuracy in predicting the bar amplitude.

C. Effects of vegetation

Bärenbold *et al.*[84] developed an analytical model for the streambed instability by applying a 2D shallow water model coupled with sediment and vegetation dynamics. In fact, effects of vegetation can be modeled as a concentrated field of rigid cylinders (non-submerged) that affect the flow by means of a roughness change. The sediment transport does not generate instabilities vigorously in the presence of substantial vegetation density owing to the vegetation-induced roughness that becomes more effective than the grain-induced roughness. A linear stability analysis of the ecomorphodynamic equations revealed that in one-dimensional framework, the instability of a straight channel produces periodic streamwise bedforms owing to an interaction between vegetation growth and mortality (through uprooting). For representative sediment transport parameters, the dominant streamwise wavelength is essentially determined by the vegetation model parameters. On the other hand, in the 2D framework, both alternate and multiple bars are found on fixed and movable beds, respectively.[84] In addition, the inclusion of the effects of vegetation to a non-vegetated streambed favors instability toward alternate bars rather than braiding.

Published under license by AIP Publishing

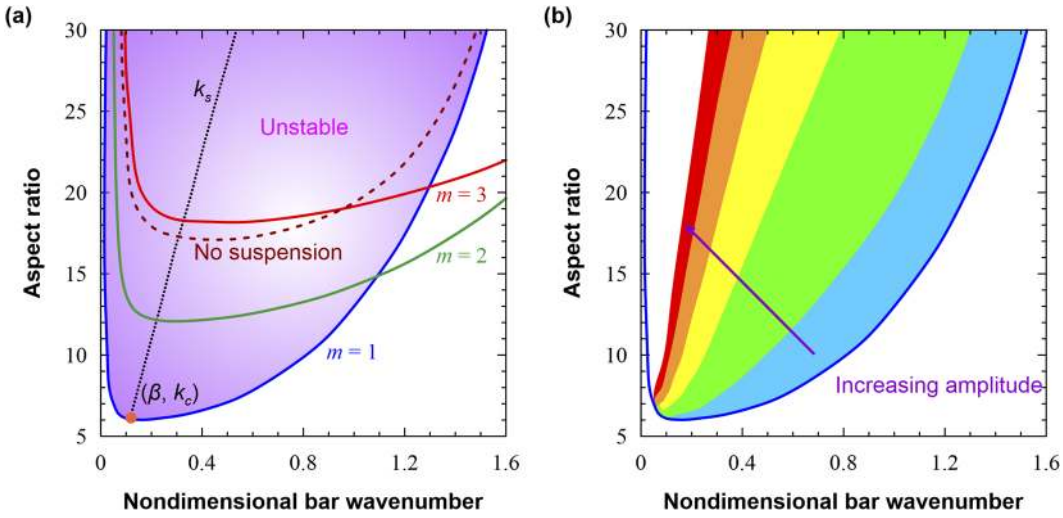

FIG. 12. Predictions of bar instability.[83] (a) Linear predictions for fundamental (m = 1) and higher (m = 2 and 3) spanwise modes. The dashed line represents the neutral stability curve without considering the role of sediment suspension. Note that the variation of k_s with β is approximately linear. (b) Nonlinear predictions. Contours of bar amplitude a_b (scaled by $2h_0$) are shown (amplitude increases from blue to red in the range of 0.05–0.25).

IV. MACRO-SCALE INSTABILITIES

In this section, macro-scale instabilities are discussed, including primarily the instability of meandering channels. Before going into its details, one fundamental aspect is to figure out the mechanism how a straight channel tends to become a meandering one. This is discussed in Subsection IV A.

A. Onset of meandering of a straight channel

Researchers proposed certain concepts in identifying the onset of meandering of a straight channel. Some of these concepts include—revolution of the Earth, streambed instability, helicoidal flow, surplus flow energy, and macro-scale turbulent eddies.[2] Importantly, Olesen[76] argued that the non-propagating alternate bars in a straight channel with erodible banks may offer an explanation for the onset of meandering. The local erosion of channel banks results in the onset of meandering and the associated curvature-induced point bars having the same wavelength. This eventually generates self-excitation initiating to meander because the curvature-induced bars stimulate the natural wavelength of non-propagating bars, being responsible for the erosion of channel banks. However, the experimental observations and the numerical modeling have evidenced that the inherent non-propagating bars can only be the predominant mechanism for the onset of meandering if the erodibility of the channel banks is mild.[77] This mechanism does not require a resonance condition or a forced steady upstream perturbation.

In a recent attempt, Dey and Ali[85] devised a thought experiment to explore the precise mechanism of the onset of meandering of a channel [Fig. 13(a)]. In the thought experiment, the motion of macro-scale turbulent eddies in a straight channel was envisioned similar to that of attached solid spheres. The spheres, initially settled in a row, are confined to parallel channel boundaries. Once the first sphere, say E_1, is given an anticlockwise rotation together with a marginal displacement toward the right-side channel boundary, the adjoining sphere E_2 is adjusted automatically as to maintain a clockwise rotation with a similar displacement toward the left-side channel boundary. The processes of alternate rotation and displacement prevail for the remaining spheres (E_3, E_4, and so on). This concept reveals that when an anticlockwise rotating macro-scale turbulent eddy E_1 in a fluvial stream removes grains from the right-side channel bank, the eroded grains are subsequently deposited at the other side of the channel bank [Fig. 13(a)]. Another macro-scale turbulent eddy E_2, next to E_1, displays a clockwise rotation with a gradual shift toward the left-side channel boundary. It therefore results in erosion and deposition of grains at left- and right-side channel boundaries, respectively. In this way, processes of alternate erosion and deposition continue, leaving a true signature of a meandering path formed by an imaginary line connecting the centers of macro-scale turbulent eddies. By applying the phenomenological theory of turbulence, Dey and Ali[85] found that at the onset of meandering, the streambed slope S_0 obeys a universal scaling law, called *Dey–Ali's law of the onset of meandering*, with channel half-width B, fluid flux Q, grain size d, and gravitational acceleration g as $S_0 \sim B^{2/9} Q^{-2/9} d^{1/3} g^{1/9}$. This scaling law has an excellent agreement with laboratory and field measurements.

B. Linear stability analysis

The dynamics of a meandering channel is inextricably linked with the instability of the erodible banks driven by the carrier fluid. Among several theories that have been developed to understand the formation of a meandering channel, the celebrated bend instability theory considers the meandering channel as a dynamic system [Fig. 1(c)], propagating and evolving in a floodplain as a result of subtle interactions of the planform, channel flow, and sediment

Published under license by AIP Publishing

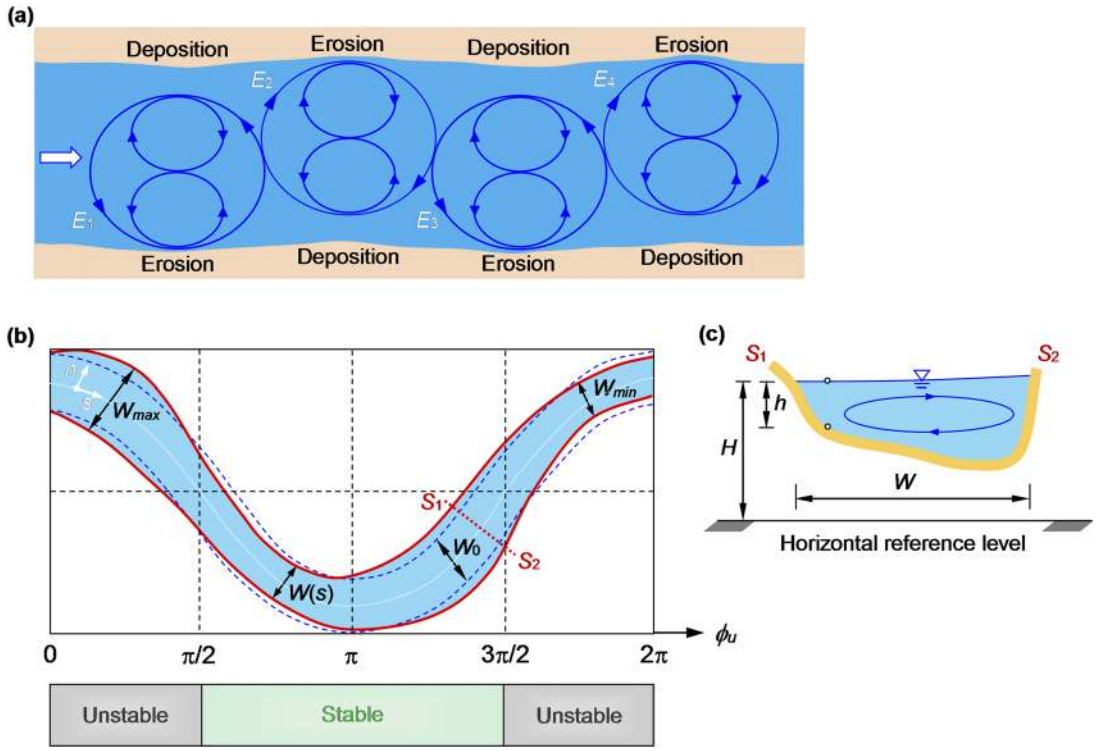

FIG. 13. (a) Thought experiment of the onset of meandering of a straight channel.[85] (b) Conceptual representation of bend instability in a meandering channel having spatial width variations. Bend instability is driven by the position of the peak spanwise migration rate. Stable and unstable regions are based on the phase lag ϕ_u between bend apex and position of the peak near-bank excess velocity. (c) Cross-sectional view of the channel at section S_1–S_2.

transport.[86] Ikeda *et al.*[86] suggested that a true meandering cannot be achieved by treating non-erodible banks that could allow the flow to follow a zigzag course around the bars [Fig. 1(b)]. Hence, they introduced the concept of bend instability, unlike the alternate-bar instability, by eliminating the non-erodible banks restraint. When the perturbations are imposed on an initially straight channel, the meandering patterns are created as a result of bank erosion.[87] The spanwise propagation of a channel is controlled by the surplus bank velocity (difference of flow velocity between outer and inner banks) and is strongly influenced by the secondary circulations emanating from the channel curvature, landscape, and channel width variations.[88,89] The linear stability analysis revealed the essential conditions for the channel bend amplitude to propagate in the spanwise direction. Ikeda *et al.*[86] found that when the channel sinuosity remains small, the bar- and bend-instability mechanisms are functioned at similar meander wavenumbers. However, it was revealed that the behavior of a meandering channel can be envisioned analogous to that of a linear oscillator, exhibiting a resonance phenomenon for some threshold values of control parameters.[87] Under the resonant condition, the channel curvature forces a natural solution, signifying a quasi-steady feature of bar perturbation. In a recent attempt, Ali and Dey[90] put forward a comprehensive description of the bend instability, considering the effects of flow regimes. The primary control parameters for the resonance phenomenon to take place were considered as the meander wavenumber, aspect ratio, Shields parameter, and relative roughness. The analysis provides an understanding of the effects of grain size on the salient features of bend instability, for instance, velocity and bed perturbations, bend amplification rate, and meandering propagation speed.

C. Effects of nonlinearity

Two fundamental aspects of meandering morphodynamics are the nonlinear and unsteady effects.[88] Among several consequences of the nonlinear effects, most remarkable ones are the upstream shifting of the position of nonlinear peak flow velocity and the damping of morphodynamic response. In the case of unsteady forcing induced by seasonal oscillations, the model results depend largely on the ratio of flood duration to morphodynamic timescale. This reveals that the system achieves a dynamic equilibrium subject to a recurring sequence of flood events. In essence, a weakly curved and long channel bend remains essentially nonlinear, implying that the bed perturbations are comparable with the mean flow depth. Although linear models have advanced the state-of-the-art significantly, they have serious limitations in capturing the salient interactions between a meandering channel and its floodplain, in conjunction with some relevant physical processes, such as bank collapse and chute cutoffs.

Published under license by AIP Publishing

Researchers reported refined treatments of spanwise bank propagation by accounting for the channel width variations.[91–96] To be specific, Parker *et al.*[92] analyzed the propagation of eroding outer bank and depositing inner bank individually. They proposed a framework to overcome the limitations of the previous approaches in modeling the propagation of meandering rivers. In fact, in several earlier models, the bank erosion rate was simply linked with some aspect of flow dynamics, and the depositing bank was considered to respond passively by propagating the amount needed to preserve a constant bank-full width. Parker *et al.*[92] specifically considered the salient roles of slump blocks (to armor the erodible banks) and vegetation (to govern the channel planform dynamics). In the long-term, they simulated a channel width, fluctuating around its mean value, aided by an insightful interaction between bar push and bank pull mechanisms. Such treatment was later tied with a fully nonlinear depth-averaged model to study the coevolution of channel width, curvature, and streambed slope over a wide range of channel width–curvature correlations, as observed in natural rivers.[96]

Let us focus on flow in a meandering channel of variable width $W(s)$ $(=2B)$, having a periodic variation with a mean W_0, with respect to the streamline coordinate system (s, n) [Fig. 13(b)]. Having denoted the velocity components as (U, V) in (s, n), we consider a specific cross section S_1–S_2 [Fig. 13(c)], where h is the local flow depth and H is the height of the free surface from a fixed reference level. Let R_0 be a characteristic length scale of the channel radius of curvature and h_0 be the section-averaged flow depth. To be specific, for a sine-generated curve, R_0 is twice the radius of curvature at the bend apex. Let us define some key parameters as follows:

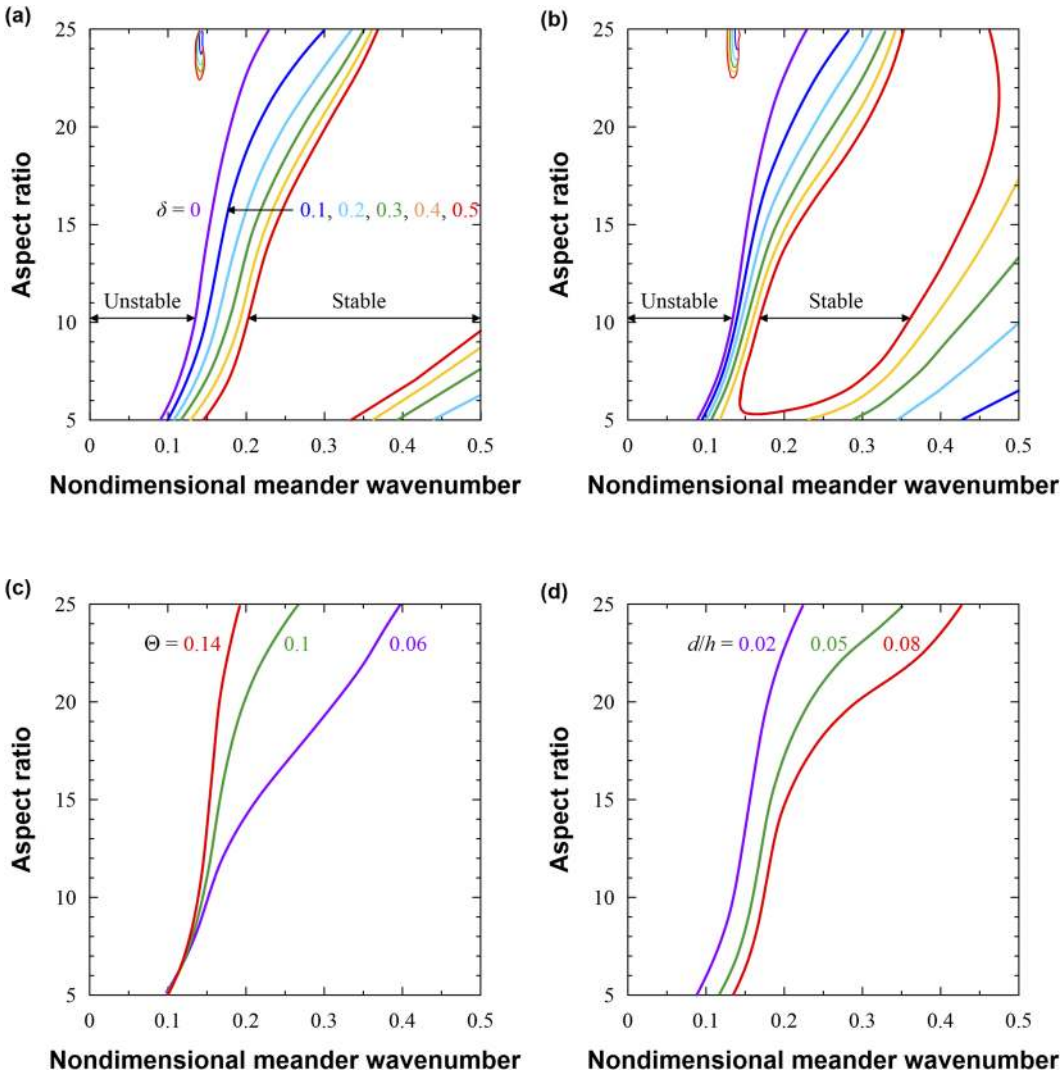

FIG. 14. Nonlinear results.[93] Effects of relative amplitude of width oscillations δ on the marginal stability curves for (a) $\omega = 0$ ($\Theta = 0.09$, $d/h = 0.03$) and (b) $\omega = -\pi/8$ ($\Theta = 0.09$, $d/h = 0.03$). Sensitivity of marginal stability curves for different values of (c) Θ ($d/h = 0.03$, $\omega = 0$, $\delta = 0.1$) and (d) d/h ($\Theta = 0.1$, $\omega = 0$, $\delta = 0.1$).

Published under license by AIP Publishing

$$\beta = \frac{W_0}{2h_0}, \quad \nu = \frac{W}{2R_0}, \quad \delta = \frac{W_{max} - W_0}{W_0}, \\ k_m = \frac{\pi W_0}{\lambda_m}, \quad \omega = -\pi(l_{W_{max}} - l_{C_{max}}), \tag{17}$$

where β denotes the aspect ratio, ν measures the variations in curvature ratio, δ defines the relative amplitude of width oscillations, k_m is the nondimensional meander wavenumber, λ_m is the meander wavelength, and ω quantifies the distance l between the widest and the most curved section. Therefore, $\omega > 0$ ($\omega < 0$) refers to the widest section being positioned upstream (downstream) of the bend apex. Denoting $(\hat{s}, \hat{n}) = (2s/W_0, 2n/W)$, the spatial variation in channel width can be set as[93]

$$\frac{W(s)}{W_0} = 1 + \delta\{1 + \exp[2i(k_m\hat{s} + \omega)] + \text{c.c.}\}. \tag{18}$$

In addition, the channel curvature can be assumed as[93]

$$\nu\mathscr{C}(s) = \nu[\exp(ik_m\hat{s}) + \exp(-ik_m\hat{s})] = \nu[e_1(\hat{s}) + \bar{e}_1(\hat{s})]. \tag{19}$$

Under these considerations, the fundamental set of variables can be expanded as

$$(\hat{U}, \hat{V}, \hat{H}, \hat{h}) = (1, 0, \hat{H}_0, 1) + \nu[(\tilde{U}_{10}, \tilde{V}_{10}, \tilde{H}_{10}, \tilde{h}_{10})e_1 + \text{c.c.}] \\ + \delta[(\tilde{U}_{01}, \tilde{V}_{01}, \tilde{H}_{01}, \tilde{h}_{01})e_2 + \text{c.c.}] \\ + \nu\delta[(\tilde{U}_{11}, \tilde{V}_{11}, \tilde{H}_{11}, \tilde{h}_{11})e_1 + \text{c.c.}], \tag{20}$$

where $(\hat{U}, \hat{V}) = (U, V)/U_0$, U_0 is the unperturbed azimuthal velocity, $\hat{H} = H/(h_0F^2)$, $F = U_0/(gh_0)^{1/2}$, $\hat{h} = h/h_0$, and variables with subscript "zero" refer to the unperturbed state. Equation (20), when substituted into the governing equations of fluid and granular motion, produces a fourth-order ordinary differential equation that can be readily solved subject to appropriate boundary conditions.[93] Introducing a phase lag ϕ_u between the bend apex and the position of the peak near-bank excess velocity, it appears that for the unstable region of a meandering channel, say $\phi_u \in (0, \pi/2)$ [Fig. 13(b)], $Re[\tilde{U}_{10} + \delta\tilde{U}_{11}(\hat{n} = 1)]$ is positive, suggesting that the spanwise propagation rate tends to grow. By contrast, for the stable region, the maximum spanwise propagation rate is located along an inner bend, say $\phi_u \in (\pi/2, 3\pi/2)$. This indicates $Re[\tilde{U}_{10} + \delta\tilde{U}_{11}(\hat{n} = 1)]$ is negative, and therefore, the meandering channel tends to become a quasi-straight channel.

Figure 14(a) shows the marginal bend curves for different values of relative amplitude of width oscillations δ in phase with curvature ($\omega = 0$). It appears that long meander bends are unstable and the range of instability expands toward larger wavenumbers, as the aspect ratio increases. On the other hand, when the widest section is located downstream ($\omega = -\pi/8$) of the bend apex [Fig. 14(b)], width variations destabilize bends with larger wavenumbers. This stabilization process depends largely on the effects of Shields parameter and relative roughness [Figs. 14(c) and 14(d)]. As the Shields parameter increases for a given aspect ratio [Fig. 14(c)], longer bends become unstable, stabilizing the shorter ones. On the other hand, smaller relative roughness (say $d/h = 0.02$) produces the instability of longer bends [Fig. 14(d)].

Linear models readily assume that the bed perturbations are quite smaller than the flow depth.[97] It turns out that the curvature-induced forcing effects are trivial to produce insignificant secondary current compared to the streamwise flow. However, in nonlinear models, the secondary currents show finite spatiotemporal variations (although slow) owing to the variations of the basic unperturbed state. Importantly, in linear models, convective effects of the lateral streamwise momentum transport (in spanwise direction) appear beyond the second order. By contrast, in nonlinear models, convective effects exist at the first order. Based on the experimental observations, Smith and Mclean[98] emphasized that the terms describing the topography-induced convective accelerations need to be incorporated at lowest order in the streamwise momentum equation. However, Bolla Pittaluga and Seminara[88] stated that the above conclusion is limited to flow in a weakly curved short channel bend and, therefore, is not universal.

D. Cutoff dynamics

In addition to local nonlinear effects that control the evolution of a meandering channel, the cutoff process essentially adds planform-scale threshold form nonlinear effects owing to the abrupt removal of bends [subpanel (ii) of Fig. 1(c)]. The local cutoffs can be envisioned as perturbations introduced to the fundamental variables that might be exaggerated driven by the nonlinear effects.[99]

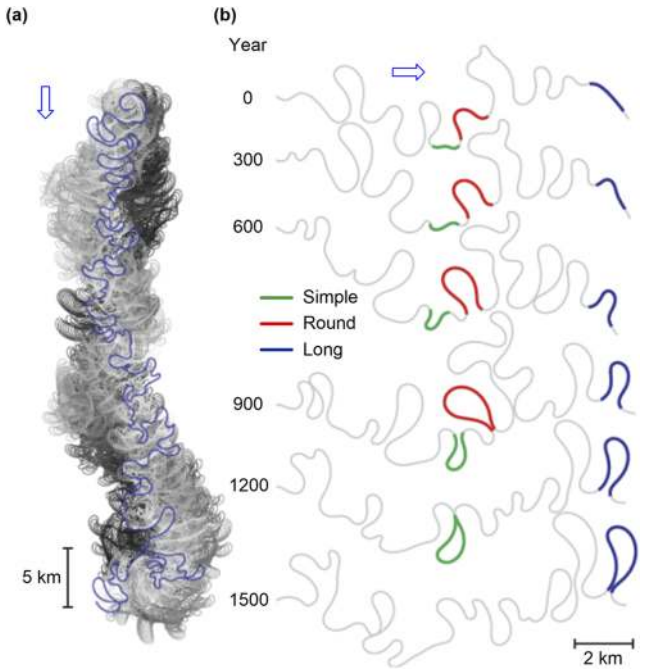

FIG. 15. Long-term simulations of a meandering river.[99] (a) Simulated centerline realizations over 30 000 years. The blue centerline corresponds to t = 30 000 years, while older centerlines are in gray. Reproduced with permission from Schwenk *et al.*, "The life of a meander bend: Connecting shape and dynamics via analysis of a numerical model," J. Geophys. Res.: Earth Surf. **120**(4), 690–710 (2015). Copyright 2015 John Wiley and Sons. (b) A reach of centerline selected realizations that are 300 years apart displays the growth and cutoff of three archetypal atoms—simple, round, and long. Reproduced with permission from Schwenk *et al.*, "The life of a meander bend: Connecting shape and dynamics via analysis of a numerical model," J. Geophys. Res.: Earth Surf. **120**(4), 690–710 (2015). Copyright 2015 John Wiley and Sons.

Published under license by AIP Publishing

Cutoffs could reduce the overall form nonlinearity by eradicating older bends.[87,100] However, they can also induce form nonlinearity, generating high-frequency scales within channel centerlines and interacting with local nonlinearities.[101]

Numerical computations over large spatiotemporal scales can effectively simulate a meandering channel over thousands of years, offering physical insights into the reach-scale measurements, for instance, mean curvature,[102] mean meander wavelength,[103] and sinuosity.[94] Schwenk *et al.*[99] presented high-fidelity temporal evolutions of individual meander bends, called atoms, from inception to cutoff (Fig. 15). Before cutoffs, the numerical simulation anticipates an archetypal simple cutoff atom. Once perturbations from cutoffs take place, two other prototypical cutoff atoms emerge, called long and round atoms. In fact, introducing three measures of meander propagation—average propagation rate, growth rate, and centroid propagation rate, it was revealed that similar cutoff atoms share similar dynamic histories. Among the dynamic measures of three distinct atoms, simple atoms have the highest growth and mean propagate rates, followed by round and long atoms. The variability in the dynamics of round atoms elucidates the impact of nearby random perturbations arising from cutoff. The precise timing of death of a given atom fundamentally depends on its dynamic history, nearby perturbations, and planimetric configuration.

V. CONCLUSIONS

This review focuses on the state-of-the-science of fluvial instabilities, illuminating their nature and underlining mechanisms from the standpoint of three characteristic scales of instability, such as micro-, meso-, and macro-scale. The key highlights of this review are as follows:

(i) In micro-scales accounting for bedform dynamics, evolutions of micro-scale instabilities are grounded on near-bed hydrodynamics, interfacial Kelvin–Helmholtz type instability, and two-stage concepts, while their driving mechanism is the phase lag between the bed movements and flow properties. The phase lag depends on some key factors, such as fluid friction, suspended sediments, gravity, and grain inertia. For subaqueous ripples, stratification effects become prominent after the formation of chevrons, particularly when the turbulent sweeps are to entrain the grains into suspension creating a heterogeneous stratified layer.

(ii) Dune instability remains convective for all the physical control parameters, whereas the antidune instability shows both convective and absolute behaviors.

(iii) In meso-scales accounting for bar dynamics, bar instability is convective in nature, even in the presence of sediment suspension. The sediment suspension is to enhance the region of bar instability by significantly reducing the threshold aspect ratio and threshold wavenumber. Sediment transport does not strongly produce instabilities in the presence of vegetation, because of the emergence of vegetation-induced roughness that dominates the grain-induced roughness. Inclusion of vegetation density to a non-vegetated streambed favors instability toward alternate bars.

(iv) In macro-scale accounting for meandering dynamics, bend instability is controlled by the position of the peak spanwise migration rate. Stable and unstable regions are distinguished with the phase lag between the bend apex and the position of the peak near-bank excess velocity. The stabilization of bends, for different relative amplitudes of width oscillations relative to curvature, depends principally on the Shields parameter and relative roughness.

(v) Local cutoffs can diminish the overall form nonlinearity by eliminating older bends, whereas they can induce form nonlinearity by producing high-frequency scales and interacting with nonlinear effects.

Despite magnificent advances in understanding the mechanisms of fluvial instabilities covering a wide range of scales, several key issues are yet to be addressed. The current research challenges of the subject are briefly outlined as follows:

(i) High-fidelity experimental data, field measurements, and numerical simulations, offering insights into the instantaneous impulsive fluid forces on sediment grains and grain–grain collisions, are to be obtained to accurately anticipate the onset of fluvial instabilities. In particular, mathematical models should stand on the 3D approach accounting for the flow separation and the near-bed complex feedback between flow and sediment transport.[67]

(ii) Precise 3D stability mechanisms of bedform amalgamation under heterogeneous grains have to be understood. The amalgamation of bedforms is vital to the development of dunes from a rippled bed. An in-depth understanding of the dynamics of coherent structures associated with the bedforms may offer new insights into this topic.[29]

(iii) Subtle effects of spatiotemporal heterogeneity and mixed-size sediments (especially the effects of vertical sorting) are to be incorporated into the theoretical models to predict the stability of gravel streambeds. In this context, the stability of bedforms in bimodal sand-gravel sediments is an important aspect.[104]

(iv) Researchers need to effectively include the role of vegetation, which provides additional bank strength, in the analytical model to further explore the mechanisms of meso- and macro-scale instabilities.

(v) Promising theoretical modeling of the precise instability mechanism of braided rivers is to be developed.

ACKNOWLEDGMENTS

S.D. acknowledges the J C Bose Fellowship Award in pursuing this work.

DATA AVAILABILITY

Data sharing is not applicable to this article as no new data were created or analyzed in this study.

REFERENCES

[1]J. G. Venditti, M. Church, and S. J. Bennett, "On interfacial instability as a cause of transverse subcritical bed forms," Water Resour. Res. **42**(7), W07423, https://doi.org/10.1029/2005wr004346 (2006).

Published under license by AIP Publishing

[2]S. Dey, *Fluvial Hydrodynamics: Hydrodynamic and Sediment Transport Phenomena* (Springer-Verlag, Berlin, Germany, 2014).
[3]S. Naqshband *et al.*, "Bed load and suspended load contributions to migrating sand dunes in equilibrium," J. Geophys. Res.: Earth Surf. **119**(5), 1043–1063, https://doi.org/10.1002/2013jf003043 (2014).
[4]Y. Ourmières and J. R. Chaplin, "Visualizations of the disturbed-laminar wave-induced flow above a rippled bed," Exp. Fluids **36**(6), 908–918 (2004).
[5]A. Recking *et al.*, "Antidunes on steep slopes," J. Geophys. Res.: Earth Surf. **114**(F4), F04025, https://doi.org/10.1029/2008jf001216 (2009).
[6]J. P. C. Eekhout, A. J. F. Hoitink, and E. Mosselman, "Field experiment on alternate bar development in a straight sand-bed stream," Water Resour. Res. **49**(12), 8357–8369, https://doi.org/10.1002/2013wr014259 (2013).
[7]J. Cisneros *et al.*, "Dunes in the world's big rivers are characterized by low-angle lee-side slopes and a complex shape," Nat. Geosci. **13**, 156–162 (2020).
[8]J. F. Kennedy, "The formation of sediment ripples, dunes, and antidunes," Annu. Rev. Fluid Mech. **1**, 147–168 (1969).
[9]J. B. Southard, "Experimental determination of bed-form stability," Annu. Rev. Fluid Mech. **19**, 423–455 (1991).
[10]F. Engelund and J. Fredsoe, "Sediment ripples and dunes," Annu. Rev. Fluid Mech. **14**, 13–37 (1982).
[11]F. Charru, B. Andreotti, and P. Claudin, "Sand ripples and dunes," Annu. Rev. Fluid Mech. **45**, 469–493 (2013).
[12]M. Church, "Bed material transport and the morphology of alluvial river channels," Annu. Rev. Earth Planet. Sci. **34**, 325–354 (2006).
[13]G. Seminara, "Fluvial sedimentary patterns," Annu. Rev. Fluid Mech. **42**, 43–66 (2010).
[14]M. G. Kleinhans, "Sorting out river channel patterns," Prog. Phys. Geogr.: Earth Environ. **34**(3), 287–326 (2010).
[15]S. Z. Ali and S. Dey, "Hydrodynamics of sediment threshold," Phys. Fluids **28**(7), 075103 (2016).
[16]S. Dey and S. Z. Ali, "Mechanics of sediment transport: Particle scale of entrainment to continuum scale of bedload flux," J. Eng. Mech. **143**(11), 04017127 (2017).
[17]S. Dey and S. Z. Ali, "Stochastic mechanics of loose boundary particle transport in turbulent flow," Phys. Fluids **29**(5), 055103 (2017).
[18]S. Dey and S. Z. Ali, "Bed sediment entrainment by streamflow: State of the science," Sedimentology **66**(5), 1449–1485 (2019).
[19]S. Z. Ali and S. Dey, "Origin of the scaling laws of sediment transport," Proc. R. Soc. A **473**, 20160785 (2017).
[20]S. Z. Ali and S. Dey, "Impact of phenomenological theory of turbulence on pragmatic approach to fluvial hydraulics," Phys. Fluids **30**(4), 045105 (2018).
[21]J. G. Venditti, M. A. Church, and S. J. Bennett, "Bed form initiation from a flat sand bed," J. Geophys. Res.: Earth Surf. **110**(F1), F01009, https://doi.org/10.1029/2004jf000149 (2005).
[22]T. Stoesser *et al.*, "Turbulence structures in flow over two-dimensional dunes," J. Hydraul. Eng. **134**(1), 42–55 (2008).
[23]A. Khosronejad and F. Sotiropoulos, "Numerical simulation of sand waves in a turbulent open channel flow," J. Fluid Mech. **753**, 150–216 (2014).
[24]F. Sotiropoulos and A. Khosronejad, "Sand waves in environmental flows: Insights gained by coupling large-eddy simulation with morphodynamics," Phys. Fluids **28**(2), 021301 (2016).
[25]E. Kwoll *et al.*, "Flow structure and resistance over subaquaeous high- and low-angle dunes," J. Geophys. Res.: Earth Surf. **121**(3), 545–564, https://doi.org/10.1002/2015jf003637 (2016).
[26]E. Kwoll *et al.*, "Observations of coherent flow structures over subaqueous high- and low-angle dunes," J. Geophys. Res.: Earth Surf. **122**(11), 2244–2268, https://doi.org/10.1002/2017jf004356 (2017).
[27]C. A. Unsworth *et al.*, "The impact of nonequilibrium flow on the structure of turbulence over river dunes," Water Resour. Res. **54**(9), 6566–6584, https://doi.org/10.1029/2017wr021377 (2018).
[28]A. Lefebvre, "Three-dimensional flow above river bedforms: Insights from numerical modeling of a natural dune field (Río Paraná, Argentina)," J. Geophys. Res.: Earth Surf. **124**(8), 2241–2264, https://doi.org/10.1029/2018jf004928 (2019).
[29]Y. Liu *et al.*, "Numerical simulation of the production of three-dimensional sediment dunes," Phys. Fluids **31**(9), 096603 (2019).
[30]S. Dey *et al.*, "Hydrodynamics of flow over two-dimensional dunes," Phys. Fluids **32**(2), 025106 (2020).
[31]H.-K. Liu, "Mechanics of sediment-ripple formation," J. Hydraul. Div. **83**(2), 1–23 (1957).
[32]Y.-J. Chou and O. B. Fringer, "A model for the simulation of coupled flow-bed form evolution in turbulent flows," J. Geophys. Res.: Oceans **115**(C10), C10041, https://doi.org/10.1029/2010jc006103 (2010).
[33]C. Escauriaza and F. Sotiropoulos, "Initial stages of erosion and bed form development in a turbulent flow around a cylindrical pier," J. Geophys. Res.: Earth Surf. **116**(F3), F03007, https://doi.org/10.1029/2010jf001749 (2011).
[34]S. E. Coleman and V. I. Nikora, "Fluvial dunes: Initiation, characterization, flow structure," Earth Surf. Processes Landforms **36**(1), 39–57 (2011).
[35]A. E. Perry, S. Henbest, and M. S. Chong, "A theoretical and experimental study of wall turbulence," J. Fluid Mech. **165**, 163–199 (1986).
[36]S. E. Coleman and B. W. Melville, "Bed-form development," J. Hydraul. Eng. **120**(5), 544–560 (1994).
[37]G. M. Ashley, "Classification of large scale subaqueous bed forms: A new look at an old problem," J. Sediment. Res. **60**(1), 160–172 (1990).
[38]J. Chabert and J. L. Chauvin, "Formation de dunes et des rides dans les modèles fluviaux," Bulletin du Centre de Recherches et d'essais de Chatou **4**, 31–51 (1963).
[39]W. Bechteler, G. Vogel, and H. J. Vollmers, "Model investigations on the sediment transport of a lower alpine river," in *Fluvial Hydraulics of Mountain Regions*, edited by A. Armanini and G. di Silvio (Springer, Berlin, Germany, 1991), pp. 769–857.
[40]D. B. Simons and E. V. Richardson, "Forms of bed roughness in alluvial channels," J. Hydraul. Div. **87**(3), 87–105 (1961).
[41]S. Naqshband *et al.*, "A sharp view on river dune transition to upper stage plane bed," Geophys. Res. Lett. **44**(22), 11437–11444, https://doi.org/10.1002/2017gl075906 (2017).
[42]G. Seminara, "Effect of grain sorting on the formation of bedforms," Appl. Mech. Rev. **48**(9), 549–563 (1995).
[43]J. Malarkey *et al.*, "The pervasive role of biological cohesion in bedform development," Nat. Commun. **6**, 6257 (2015).
[44]D. R. Parsons *et al.*, "The role of biophysical cohesion on subaqueous bed form size," Geophys. Res. Lett. **43**(4), 1566–1573, https://doi.org/10.1002/2016gl067667 (2016).
[45]J. H. Baas *et al.*, "Integrating field and laboratory approaches for ripple development in mixed sand-clay-EPS," Sedimentology **66**(7), 2749–2768 (2019).
[46]F. M. Exner, "Über die wechselwirkung zwischen wasser und geschiebe in flüssen," Sitzungsber Akad. Wiss. **134**(2a), 165–203 (1925).
[47]S. Dey, S. Z. Ali, and E. Padhi, "Bedload transport from analytical and turbulence phenomenological perspectives," Int. J. Sediment Res. **34**(6), 509–530 (2019).
[48]S. Dey, S. Z. Ali, and E. Padhi, "Advances in analytical modeling of suspended sediment transport," J. Hydro-Environ. Res. **20**, 110–126 (2018).
[49]C. C. S. Song, "Modified kinematic model: Application to bed forms," J. Hydraul. Eng. **109**(8), 1133–1151 (1983).
[50]F. Núñez-González and J. P. Martín-Vide, "Analysis of antidune migration direction," J. Geophys. Res.: Earth Surf. **116**(F2), F02004, https://doi.org/10.1029/2010jf001761 (2011).
[51]J. F. Kennedy, "The mechanics of dunes and antidunes in erodible-bed channels," J. Fluid Mech. **16**, 521–544 (1963).
[52]T. Hayashi, "Formation of dunes and antidunes in open channels," J. Hydraul. Div. **96**(2), 357–366 (1970).
[53]S. K. Bose and S. Dey, "Reynolds averaged theory of turbulent shear flows over undulating beds and formation of sand waves," Phys. Rev. E **80**(3), 036304 (2009).
[54]R. A. Callander, "Instability and river channels," J. Fluid Mech. **36**, 465–480 (1969).
[55]J. D. Smith, "Stability of a sand bed subjected to a shear flow of low Froude number," J. Geophys. Res.: Oceans Atmos. **75**(30), 5928–5940, https://doi.org/10.1029/jc075i030p05928 (1970).
[56]K. J. Richards, "The formation of ripples and dunes on an erodible bed," J. Fluid Mech. **99**, 597–618 (1980).

Published under license by AIP Publishing

[57]B. M. Sumer and M. Bakioglu, "On the formation of ripples on an erodible bed," J. Fluid Mech. **144**, 177–190 (1984).
[58]M. Colombini, "Revisiting the linear theory of sand dune formation," J. Fluid Mech. **502**, 1–16 (2004).
[59]F. Charru and E. J. Hinch, "Ripple formation on a particle bed sheared by a viscous liquid. Part 1. Steady flow," J. Fluid Mech. **550**, 111–121 (2006).
[60]F. Charru and E. J. Hinch, "Ripple formation on a particle bed sheared by a viscous liquid. Part 2. Oscillating flow," J. Fluid Mech. **550**, 123–137 (2006).
[61]M. Colombini and A. Stocchino, "Three-dimensional river bed forms," J. Fluid Mech. **695**, 63–80 (2012).
[62]F. Engelund, "Instability of erodible beds," J. Fluid Mech. **42**, 225–244 (1970).
[63]J. Fredsøe, "On the development of dunes in erodible channels," J. Fluid Mech. **64**, 1–16 (1974).
[64]S. K. Bose and S. Dey, "Instability theory of sand ripples formed by turbulent shear flows," J. Hydraul. Eng. **138**(8), 752–756 (2012).
[65]M. Colombini and A. Stocchino, "Ripple and dune formation in rivers," J. Fluid Mech. **673**, 121–131 (2011).
[66]A. Fourrière, P. Claudin, and B. Andreotti, "Bedforms in a turbulent stream: Formation of ripples by primary linear instability and of dunes by nonlinear pattern coarsening," J. Fluid Mech. **649**, 287–328 (2010).
[67]O. Duran Vinent *et al.*, "A unified model of ripples and dunes in water and planetary environments," Nat. Geosci. **12**, 345–350 (2019).
[68]G. Parker, "Sediment inertia as cause of river antidunes," J. Hydraul. Div. **101**(2), 211–221 (1975).
[69]B. Andreotti *et al.*, "Bedforms in a turbulent stream: Ripples, chevrons and antidunes," J. Fluid Mech. **690**, 94–128 (2012).
[70]R. Vesipa *et al.*, "On the convective-absolute nature of river bedform instabilities," Phys. Fluids **26**(12), 124104 (2014).
[71]P. Bohorquez and C. Ancey, "Stochastic-deterministic modeling of bed load transport in shallow water flow over erodible slope: Linear stability analysis and numerical simulation," Adv. Water Resour. **83**, 36–54 (2015).
[72]C. A. Alvarez and E. M. Franklin, "Role of transverse displacements in the formation of subaqueous barchan dunes," Phys. Rev. Lett. **121**(16), 164503 (2018).
[73]A. Khosronejad and F. Sotiropoulos, "On the genesis and evolution of barchan dunes: Morphodynamics," J. Fluid Mech. **815**, 117–148 (2017).
[74]C. Camporeale and L. Ridolfi, "Modal versus nonmodal linear stability analysis of river dunes," Phys. Fluids **23**(10), 104102 (2011).
[75]A. Crosato and E. Mosselman, "An integrated review of river bars for engineering, management and transdisciplinary research," Water **12**(2), 596 (2020).
[76]K. W. Olesen, "Alternate bars in and meandering of alluvial rivers," in *River Meandering, Proceedings of the Conference Rivers 1983*, edited by C. M. Elliott (American Society of Civil Engineers, 1984), pp. 873–884.
[77]A. Crosato *et al.*, "Experimental and numerical evidence for intrinsic nonmigrating bars in alluvial channels," Water Resour. Res. **47**(3), W03511, https://doi.org/10.1029/2010wr009714 (2011).
[78]M. Colombini, G. Seminara, and M. Tubino, "Finite-amplitude alternate bars," J. Fluid Mech. **181**, 213–232 (1987).
[79]M. Tubino, "Growth of alternate bars in unsteady flow," Water Resour. Res. **27**(1), 37–52, https://doi.org/10.1029/90wr01699 (1991).
[80]B. Federici and G. Seminara, "On the convective nature of bar instability," J. Fluid Mech. **487**, 125–145 (2003).
[81]B. Federici and G. Seminara, "Effect of suspended load on sandbar instability," Water Resour. Res. **42**(7), W07407, https://doi.org/10.1029/2005wr004399 (2006).
[82]M. Bolla Pittaluga and G. Seminara, "Depth-integrated modeling of suspended sediment transport," Water Resour. Res. **39**(5), 1137, https://doi.org/10.1029/2002wr001306 (2003).
[83]M. B. Bertagni and C. Camporeale, "Finite amplitude of free alternate bars with suspended load," Water Resour. Res. **54**(12), 9759–9773, https://doi.org/10.1029/2018wr022819 (2018).
[84]F. Bärenbold, B. Crouzy, and P. Perona, "Stability analysis of ecomorphodynamic equations," Water Resour. Res. **52**(2), 1070–1088, https://doi.org/10.1002/2015wr017492 (2016).
[85]S. Dey and S. Z. Ali, "Origin of the onset of meandering of a straight river," Proc. R. Soc. A **473**, 20170376 (2017).
[86]S. Ikeda, G. Parker, and K. Sawai, "Bend theory of river meanders. Part 1. Linear development," J. Fluid Mech. **112**, 363–377 (1981).
[87]G. Seminara, "Meanders," J. Fluid Mech. **554**, 271–297 (2006).
[88]M. Bolla Pittaluga and G. Seminara, "Nonlinearity and unsteadiness in river meandering: A review of progress in theory and modelling," Earth Surf. Processes Landforms **36**(1), 20–38 (2011).
[89]G. Zolezzi, R. Luchi, and M. Tubino, "Modeling morphodynamic processes in meandering rivers with spatial width variations," Rev. Geophys. **50**(4), RG4005, https://doi.org/10.1029/2012rg000392 (2012).
[90]S. Z. Ali and S. Dey, "Hydrodynamic instability of meandering channels," Phys. Fluids **29**(12), 125107 (2017).
[91]S. E. Darby, A. M. Alabyan, and M. J. Van de Wiel, "Numerical simulation of bank erosion and channel migration in meandering rivers," Water Resour. Res. **38**(9), 2-1–2-21, https://doi.org/10.1029/2001wr000602 (2002).
[92]G. Parker *et al.*, "A new framework for modeling the migration of meandering rivers," Earth Surf. Processes Landforms **36**(1), 70–86 (2011).
[93]R. Luchi, G. Zolezzi, and M. Tubino, "Bend theory of river meanders with spatial width variations," J. Fluid Mech. **681**, 311–339 (2011).
[94]A. Frascati and S. Lanzoni, "A mathematical model for meandering rivers with varying width," J. Geophys. Res.: Earth Surf. **118**(3), 1641–1657, https://doi.org/10.1002/jgrf.20084 (2013).
[95]E. C. Eke *et al.*, "Coevolution of width and sinuosity in meandering rivers," J. Fluid Mech. **760**, 127–174 (2014).
[96]E. Eke, G. Parker, and Y. Shimizu, "Numerical modeling of erosional and depositional bank processes in migrating river bends with self-formed width: Morphodynamics of bar push and bank pull," J. Geophys. Res.: Earth Surf. **119**(7), 1455–1483, https://doi.org/10.1002/2013jf003020 (2014).
[97]H. Johannesson and G. Parker, "Linear theory of river meanders," in *River Meandering*, edited by S. Ikeda and G. Parker (American Geophysical Union, Washington, DC, 1989), Vol. 12, pp. 181–214.
[98]J. D. Smith and S. R. Mclean, "A model for flow in meandering streams," Water Resour. Res. **20**(9), 1301–1315, https://doi.org/10.1029/wr020i009p01301 (1984).
[99]J. Schwenk, S. Lanzoni, and E. Foufoula-Georgiou, "The life of a meander bend: Connecting shape and dynamics via analysis of a numerical model," J. Geophys. Res.: Earth Surf. **120**(4), 690–710, https://doi.org/10.1002/2014jf003252 (2015).
[100]C. Camporeale, E. Perucca, and L. Ridolfi, "Significance of cutoff in meandering river dynamics," J. Geophys. Res.: Earth Surf. **113**(F1), F01001, https://doi.org/10.1029/2006jf000694 (2008).
[101]J. Schwenk and E. Foufoula-Georgiou, "Are process nonlinearities encoded in meandering river planform morphology?," J. Geophys. Res.: Earth Surf. **122**(8), 1534–1552, https://doi.org/10.1002/2016jf003929 (2017).
[102]A. D. Howard and A. T. Hemberger, "Multivariate characterization of meandering," Geomorphology **4**(3-4), 161–186 (1991).
[103]C. Camporeale *et al.*, "On the long-term behavior of meandering rivers," Water Resour. Res. **41**(12), W12403, https://doi.org/10.1029/2005wr004109 (2005).
[104]R. A. Kuhnle *et al.*, "Bed forms in bimodal sand-gravel sediments: Laboratory and field analysis," Sedimentology **53**(3), 631–654 (2006).

Published under license by AIP Publishing